X-ray spectroscopic and scattering methods applied to the characterisation of Cobalt-based Fischer-Tropsch Synthesis catalysts

Jennifer J. Herbert[a,b,c], Pierre Senecal[a,b], David J. Martin[a,b], Wim Bras[c], Simon K. Beaumont[d] and Andrew M. Beale[a,b]

[a] *Department of Chemistry, University College London, 20 Gordon Street, London, WC1H 0AJ, UK*

[b] *UK Catalysis Hub, Research Complex at Harwell, Harwell, Didcot, Oxfordshire OX11 0FA, UK*

[c] *Netherlands Organisation for Scientific Research (NWO), DUBBLE CRG@ESRF, Grenoble 38042, France*

[d] *Department of Chemistry, University of Durham, Durham, DH1 3LE, UK*

Abstract: This review aims to critically assess the use of X-ray techniques, both of a scattering (e.g. X-ray diffraction (XRD), Pair Distribution Function (PDF)) and spectroscopic nature (X-ray Absorption spectroscopy (XAFS)), in the study of cobalt-based Fisher-Tropsch Synthesis (FTS) catalysts. In particular, the review will focus on how these techniques have been successfully used to describe the salient characteristics of these catalysts that govern subsequent activity and selectivity, as well as to afford insight into deactivation phenomena that have seemingly stifled their application. We discuss how these X-ray-based techniques have been used to yield insight into the bulk structure, the catalyst surface, oxidation states, local (cobalt) geometry, and elemental composition of particles, primarily from a 1D perspective but we also highlight how, with recent developments in advanced X-ray characterisation methods, crucial information can now be obtained in 2D and 3D. The examples chosen focus on data acquired *in situ/operando*, under realistic operating conditions and during activation which often allow for obtaining a more relevant perspective on the changes in catalyst structure that accompany a change in catalyst performance. We conclude with a perspective on some of the challenges that beset the Co-based FTS technology and discuss how X-ray based techniques could be used to solve them.

Contents

I. Introduction

In recent years, the century-old Fischer-Tropsch synthesis (FTS) has experienced something of a renaissance due to expected long term increases in oil price, traditional fuel supply concerns and environmental factors. It has also attracted significant investment due to advances in the extraction of natural gas, recent legislation and the increasing interest in the possibility to use syngas derived from partial combustion or pyrolysis of biomass. [1] FTS is an essential industrial process which produces long alkanes, alkenes or alcohols using synthetic gas (syngas; a CO/H_2 gas mixture) which is produced from the gasification of methane, coal or biomass. This method of synthesis provides ultra-clean fuels (without sulfur, nitrogen or aromatic poisons) that could be substituted for gasoline or diesel fuel produced in the refinery, therefore representing one possible ways to replace dwindling oil resources, especially as drop-in replacements for transport fuels. FTS proceeds via a hydrogenation reaction to form olefins and alkanes:

Olefin formation: $n\mathrm{CO} + 2n\ \mathrm{H_2} \rightarrow \mathrm{C}_n\mathrm{H}_{2n} + n\mathrm{H_2O}$ (1)

Alkane formation: $n\mathrm{CO} + (2n+1)\ \mathrm{H_2} \rightarrow \mathrm{C}_n\mathrm{H}_{2n+2} + n\mathrm{H_2O}$ (2)

FTS plays a significant role in gas-to-liquids (GTL) technology. The GTL process as a whole is comprised of three main stages; the first being the generation of syngas from natural gas via partial oxidation or autothermal reforming, the second is FTS itself, and the final stage is the refinement or upgrading of synthetic crude oil (syncrude) produced by FTS into gas-oil (80 %) and naphtha (20 %) [2]. Cobalt catalysts are chosen for FTS reactions which use an ideal syngas ratio of $H_2/CO = 2$ (typically syngas derived from natural gas), as Co is significantly less reactive in the water-gas shift (WGS) reaction. [3] Whereas, Fe catalysts exhibit strong activity in WGS, which is used alongside FTS in reactors to compensate for the less than ideal CO-rich syngas. [4]

Cobalt-based FTS catalysts are usually comprised of cobalt in its metallic form (Co^0), dispersed as small particles on an oxide (Al_2O_3, SiO_2 and TiO_2) or a microporous/mesoporous support [5]. Co^0 particles are believed to be the primary active sites as the metallic Co is present throughout FTS [4]. Other cobalt species found in FTS catalysts include; cobalt oxide (both CoO and Co_3O_4), cobalt carbide (Co_2C) and cobalt-supported compounds (such as cobalt aluminate ($CoAl_2O_4$) or cobalt titanate ($CoTiO_3$)) [6]. The oxidation of cobalt catalysts by water to form cobalt oxides, first raised as an issue in work by A. Holmen [7], has been

extensively discussed in the literature as research groups strive to determine whether oxidation is in fact a catalytic deactivation mechanism [7,8]. In the past, it has been assumed that oxidation triggers deactivation but XAFS measurements have suggested that water oxidation may not be an issue for these catalyst [9]. As a direct result of the high cost of cobalt, optimized dispersion of the nanoparticles is required to facilitate lower catalyst loadings. [4] In order to achieve this, methods of synthesis have been developed/tailored in order to more tightly control the size of the metallic cobalt nanoparticles. For example, the addition of promotors or additional chemicals to the impregnating solution containing the precursor of $Co(NO_3)_2$ has been shown to enhance the catalyst performance either by improved control of the metal support interaction, or improved control of the size of metallic cobalt nanoparticles formed after activation. [10,11] Studies using catalysts prepared by well-known catalyst preparation methods (i.e. incipient wetness impregnation (IWI)) [12] as well as model catalyst systems utilising size-controlled nanoparticles have generally indicated large nanoparticles above around 6 nm to be optimal [12–14]. This particle size dependence has been attributed to a higher quantity of low-coordinated Co surface sites on particles of less than 6 nm as larger CH_x residence times and lower CH_x coverage have been observed by Steady-State Isotopic Transient Kinetic Analysis (SSITKA). [11]

Diverse X-ray scattering and spectroscopic methods are employed to understand the stages involved in the creation and application of active cobalt-based FTS catalysts, the origins of activity, and possible mechanisms of deactivation. Due to the energy dependant interaction of electromagnetic radiation with common matter, X-rays can be used to investigate bulk/surface properties, crystallinity (or lack thereof), element specific features, or all the aforementioned properties combined in certain coupled systems. Notably, X-ray scattering techniques find their main utility in studies of the cobalt catalyst itself, which make such techniques highly complementary to a variety of both optical techniques (Raman and infra-red (IR)) and adsorption-desorption techniques (notably SSITKA [11]), used for the study of the reactive adsorbates. This is demonstrated with carefully selected examples herein.

II. X-Ray scattering techniques as applied to Co-based FT catalysts

Scattering methods provide vital insight into the structure of Co-based FT catalysts and the structural changes that occur over the course of catalyst formation and FTS. There are a variety of X-ray scattering techniques available which can probe a wide range of length scales. This ranges from the long range (XRD for crystalline phase information), intermediate range (SAXS for morphology change), and short range (PDF for determining the presence of diffraction silent material such as amorphous Co/C deposition).

II.1. Powder X-Ray Diffraction (PXRD)

Powder X-Ray diffraction (PXRD) examines X-rays scattered from the ordered material present in a powder sample at angles characteristic of the crystal lattices present caused by constructive X-ray interference between the atomic planes. [15] The XRD data can be analyses to obtain information on the phases' present and crystallite sizes (most commonly by Rietveld refinement). [16] PXRD is particularly relevant for the characterisation of FT catalysts due to the relatively large metal loadings leading to sufficient ordering of nanoparticles to render them readily identifiable (particularly in terms of phase composition and 'critical' particle size).

Operando and *in situ* measurements are frequently performed using SR due to the sufficient time resolution available. Other advantages of using synchrotron-based PXRD include that measurements can be obtained in combination with other techniques such as XAS or used for multi-dimensional imaging. The majority of laboratory-based XRD measurements are typically performed *ex situ*, however operando measurements are achievable using such set-ups and can allow for the study of catalysts with considerably more time on stream. [17] *Ex situ* measurements are much more straightforward to acquire and can provide useful information, either on their own [18] or by comparing results with *in situ* measurements from capillary reactors [19]. Simple *ex situ* lab-based XRD is widely used to compare how the crystallite size and the cobalt phases (Co_3O_4, CoO, and both hcp/fcc Co^0) vary with factors thought to affect the catalysts. For example, hydrocarbon selectivity of cobalt on various supports (γ-Al_2O_3, θ-Al_2O_3, δ-Al_2O_3 and α-Al_2O_3) [20], the syngas ratio (H_2:CO; 1:1, 2:1, and 3:1) [21] and various deactivation mechanisms such as; sulfur poisoning, catalyst sintering and silicate and/or carbide formation [18]. However, it should be

noted at this stage that many lab-based PXRD apparatus utilise Cu targets often without a secondary monochromator which leads to an increased background in the measured data caused by Co fluorescence which can obscure impurity phases and renders detailed sample analysis difficult. In contrast, SR-based PXRD facilities, typically possess a combination of high photon source brightness, energy tunabilitiy and are equipped with superior detectors, enabling the collection of high quality data with superior temporal and in some cases high spatial resolution under both *in situ* and *operando* conditions [22,23]. Such *in situ* methods can also be combined with spectroscopic techniques such as XAFS and in some instances with optical methods such as UV-Vis spectroscopy or more commonly, Raman scattering [24].

Phases commonly detected by XRD in cobalt-based FT catalysts and their crystallographic structures are summarised in table 1.

Table 1: Common crystallographic phases observed in cobalt-based FT catalysts. [25–29]

Cobalt Compound	**Form**	**Crystallographic Structure**							
		Space Groups	**Lattice Parameters**						**Units per cell**
			a(Å)	***b(Å)***	***c(Å)***	***α(°)***	***β(°)***	***γ(°)***	
Co^0	hcp	P63/mmc(194)	2.5054	2.5054	4.0893	90	90	120	2
	fcc	Fm-3m(225)	3.5441	3.5441	3.5441	90	90	90	4
CoO	Rocksalt Structure	Fm-3m(225)	4.263	4.263	4.263	90	90	90	4
Co_3O_4	Normal Spinel	Fd-3mS(227)	8.065	8.065	8.065	90	90	90	8
Co_2C	Hexagonal structure	Pmnn(58)	2.8969	4.4465	4.3707	90	90	90	2
$CoAl_2O_4$	Normal Spinel	Fd-3mS(227)	8.095	8.095	8.095	90	90	90	8

In situ SR PXRD measurements can be acquired with a time resolution ranging from milliseconds to minutes, thereby allowing for the acquisition of a series of PXRD patterns as time progresses throughout activation or a FTS reaction. [6] This allows for the tracking of crystalline phase changes with time, and importantly, variation in crystallite size – yielding valuable information on the system and its evolution with time under a controlled atmosphere.

Characterisation of Co FTS catalysts using *in situ* PXRD (and indeed *in situ* XAFS or combined studies) is best performed using glass or quartz capillaries which can be envisaged as plug-flow micro-reactors. This is in contrast to the use of pelletised wafers which are easier to interrogate with analytical methods, but which are susceptible to problems with gas-

diffusion [15] Sample loadings applied are typically of the order of a few mg thereby enabling the gas delivery system to deliver flows of the order of ml/min which is very much in the order of the weight hourly space velocities (WHSV) and gas hourly space velocities (GHSV) reported for FTS experiments [30]. For example, 50 ml/min (STP) mass flow, in a reactor with 50 mg of catalyst would equal a WHSV of 26 h^{-1}, and yield products such as propene at 1 bar pressure. Ideally, *in situ/operando* experiments use similar reaction conditions for FTS to those used industrially (T ≈ 473-523 K, P ≈ 20 bar, syngas ratio of $H_2/CO \approx 2$ [31–33]), comparable to conditions in fixed bed reactors [34]. Sample environments as described above have been commissioned at the ESRF on both the Swiss-Norwegian Beamline (SNBL) and the Dutch-Belgian Beamline (DUBBLE), and are described in detail elsewhere. [35,36]

Common pre-treatment methods involve the reduction of Co_3O_4 particles (produced by the chosen preparation method), to the active species of metallic cobalt in a flow of H_2. The reduction path from Co_3O_4 to metallic Co has been shown to proceed via CoO [4]. Typically, both fcc and hcp Co^0 are present in Co-based catalysts (to varying degrees) depending on the synthesis method and the particle size (fcc being more dominant in Co particles <10 nm).

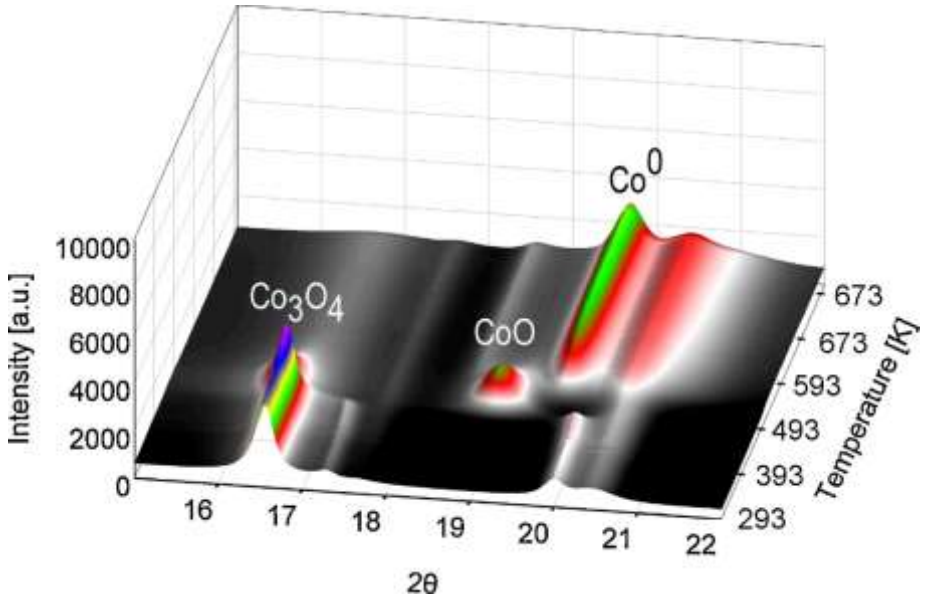

Figure 1: *In situ* PXRD patterns from reduction study of Re promoted Co/γ-Al_2O_3, recorded using a wavelength of 0.70417 Å. The samples were heated from 293 K to 673 K at 3 K/min. The data contain reflections corresponding to Co_3O_4 (311) at 16.54° 2θ, CoO (111) at 18.93° 2θ, and Co^0 (111) at 20.44° 2θ attributed to fcc and hcp. Reproduced with permission from Elsevier, Ronning et al. Catalysis Today 155 (2010) 289–295 [34].

In Figure 1 the evolution of the PXRD pattern during reduction of a Re promoted Co/γ-Al_2O_3 catalyst (20 wt%), reduced in a flow of H_2 at a pressure of 10 bar gas pressure is shown. [34]. It can be seen that initially a Co_3O_4 reflection (311) was detected at 16.54° 2θ, which then disappears at 483 K, accompanied by the emergence of a CoO peak at 18.93° 2θ. The CoO peak then in turn disappears and a Co^0 peak at 20.44° 2θ is then detected [34]. The diffraction patterns in this study contain diffraction peaks which correspond to both fcc and hcp Co^0. Naturally it is difficult to ascertain the location and quantity of the two metallic phases without further analysis (i.e. Rietveld), as many of the diffraction peaks of the various Co-containing phases (and supports) overlap which is a particular problem for nanoparticulate systems possessing broad diffraction peaks.

Although activation studies show the greatest variation in structure, *operando* studies of FTS itself provide insight into and the most relevant information to the actual process. For example, *operando* PXRD measurements were performed by Sadeqzadeh *et al.* in combination with XAFS measurements. [37] Full profile matching was used to determine the size of the Co^0 crystallites and the behaviour of the variation in size throughout FTS was studied for various syngas ratios. Sadeqzadeh *et al.* observed an increase in crystallite size over the first 140 min of the reaction in all their samples, which they attributed to sintering of the Co^0 particles during the initial phase of FTS. However, this could also be due to the continued reduction of a partially reduced catalyst under FTS conditions. This effect is most pronounced in the sample treated with higher syngas ratios although most noticeable in the sample treated in $H_2/CO = 2$. Similar Co^0 crystallite behaviour was observed in the Rønning *et al.* study described above and Karaca *et al*. [31,34] A drawback of *operando* experiments performed at industrially relevant pressures (~ 20 bar gas pressure), is the production of waxes. This production of waxes during *operando* studies is often problematic as capillaries with small diameters (~ 0.5 – 2 mm), are required to give good quality diffraction data, which are easily blocked by wax resulting in studies with short times on stream (< 4 h). This build-up of wax can often be observed in *operando* diffraction patterns as an amorphous peak at low angles (~ 6 – 8 °2θ). [34,37]

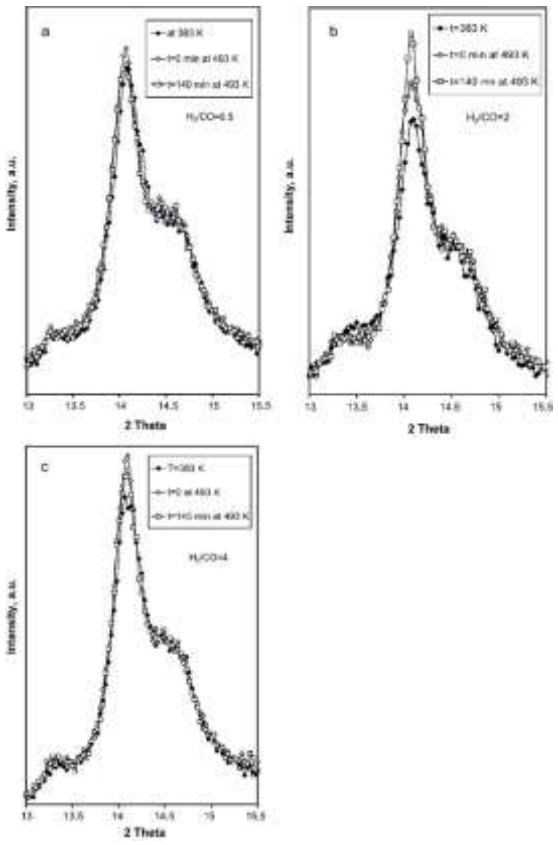

Figure 2: XRPD diffraction patterns of $CoPt/Al_2O_3$ catalysts under syngas at a pressure of 20 bar. All three frames display diffraction patterns before the temperature ramp to FTS conditions, at the beginning of FTS and after ~140 min. Of various syngas ratios a) H_2/CO = 0.5 b) H_2/CO = 2 and c) H_2/CO = 4. Reproduced with permission from Elsevier, Sadeqzadeh et al. Catal. Today. 164 (2011) 62–67[37]

The bulk Co_2C phase is also detectable by PXRD, the formation of which is believed to be a mechanism of deactivation of FT catalysts. A notable example of this was reported by Karaca *et al*. Co_2C was detected in platinum promoted Co/Al_2O_3 samples (5 wt%) studied under FTS conditions of T = 493 K, P = 20 bar and H_2/CO = 2 after a time on stream of > 8 h [38]. Small diffraction peaks that were attributable to a Co_2C phase emerged after 8-10 h and were accompanied by a decrease in the intensity of metallic cobalt peaks [38]. Cobalt sintering was also detected within the first 3 – 5 h of FTS, demonstrated by an increase in the mean size of the fcc Co crystallites from 6 to 10 nm for samples calcined at 573 K and 5.3 to 6.5 nm in those calcined at 773 K [38].

In situ and *ex situ* studies both involve some degree of compromise. Most *in situ* FTS studies last only a few hours per sample, covering primarily the initial stages of FTS and are therefore are unable to examine any long-term deactivation. Whereas *ex situ* measurements of spent FTS catalyst from a reactor risk exposing the air sensitive sample to air. In this manner it is possible to characterise a catalyst that has been online significantly longer and in a more realistic reactor, allowing longer term deactivation to occur. For example, Tsakoumis *et al*. studied spent catalysts that had been on stream in the reactor for 100 hours [33]. The study performs a comparison of crystallite particle size of the fcc Co^0 determined by PXRD for a Re promoted Co/Al_2O_3 catalyst after *in situ* PXRD of FTS (30 h on stream) in a micro plug flow reactor, pseudo *in situ* treatment in a fixed bed reactor (FBR) for 100 h. The average crystallite size of the fcc Co^0 of the sample run for 100 h (6.9 nm) in the FBR is smaller than that of those tested in the *in situ* cell (8.6 nm), which they attribute to the passivation of the wax embedded spent catalyst. The results from the latter study closely mirrors the size of the initially reduced sample (8.5 nm). This highlights the need to test catalysts under realistic conditions. Although this review focuses on synchrotron-based studies laboratory-based XRD *in situ/operando* studies are very much achievable and have been performed notably by Cats *et al*. and Fischer *et al*. [17,39] Although they lack the high spatial and time resolution of synchrotron-based XRD studies lab-based studies can run for significantly longer times, studying the phase behaviour of the crystalline material further into the reaction itself.

Although Co^0 is presumed to be the active site for FTS, it has been observed that there are notable differences between the catalytic performances of the fcc and hcp structures of Co, with some studies suggesting that the hcp form is more active [37]. Most notably, this issue was explored by Ducreaux *et al.* in 2008. [40] In this study, catalysts were modified after synthesis to produce metallic Co phases with one polymorph (hcp or fcc) dominant, whilst maintaining the consistency of the other catalyst parameters. Hcp structures were achieved by carbonization of Co^0 under CO at 230 °C followed by a decomposition to Co^0 under H_2 at 230 °C. XRD patterns of these catalysts were recorded and modelled computationally to confirm in fact the fcc and hcp Co^0 (both clearly present in the material from the diffraction patterns), are stacked within the particles as a complex succession of stacking faults (as opposed to individual hcp and fcc particles). Catalytic testing was then carried out on the respective catalysts, which found that although product selectivity was comparable, the hcp-containing catalyst had a 50 % higher conversion rate. [40] It has been suggested that this is due to either the differing reducibility of fcc and hcp cobalt or the structural stacking exhibited within fcc Co, which is surface defect deficient. Surface defect

sites such as kinks and steps have beeen shown via DFT calculations to allow carbon monoxide (CO) and other gas molecules to bind to the site more easily [41]. The high binding energy possibly encourages CO dissociation and consequently increases the FTS turnover rate [42].

Many SR-based studies have had difficulties evaluating the extent to which fcc vs hcp Co^0 are present in FTS catalysts, mainly due to reflection overlap between the various Co-containing phases and also with reflections originating from the support phase. It is worth noting, however, that techniques such as spin-echo NMR could be used for hcp vs fcc quantification purposes and which would be very powerful if used in conjunction with *in situ* XRD. In one study, NMR on ^{59}Co nuclei in Co/UPTFE (ultra-dispersed poly(tetrafluoroethene)) samples has been reported. Co in hcp and fcc structures have different environments and so appear in spin-echo NMR as two Gaussian curves at different signal frequencies. [43] The ratio was determined by comparing the areas of the Gaussian fits of the two peaks corresponding to hcp and fcc Co^0 respectively. The percentage values were fcc 16 ± 3 % and hcp 84 ± 3 %, however these samples are supported on a UPTFE support with distinctly different behaviour to the metal oxides commonly used for FT catalysts.

II.2. Total Scattering or Pair Distribution Function Analysis (PDF)

Total scattering presents the opportunity to examine FTS catalysts over many length scales simultaneously and independent of ordering. This is achieved by analysing the diffuse scattering, detecting all of the cobalt content as well as the support contribution regardless of crystallinity or particle size. Briefly, total scattering data is analysed though the reduced structure factor, F(Q) = Q[S(Q)-1], extracted from the scattering pattern, where S(Q) is the total scattering function [44]. The pair distribution function (PDF) is obtained by performing a Fourier transform on F(Q). Numerically the PDF equation is obtained using equation (3), where Q is the momentum transfer vector [45].

$$G(r) = \frac{2}{\pi}\int_0^\infty Q[S(Q) - 1]\sin(Qr)\,dQ, \qquad (3)$$

The PDF represents the probability of finding two atoms separated by a distance in real space *r*. Unlike diffraction, PDF data is analysed in real space rather than in reciprocal space. Structural information on the system can be extracted from the PDF by structural modelling or even by simple analysis of the peak positions [46]. Total scattering requires

similar beam and detector properties to other scattering techniques, however for detailed analysis a particularly high Q-range of ca. >20 $Å^{-1}$ is required which favours the use of short X-ray wavelengths. Although neutron PDF has been in use for a long time X-ray PDF is a relatively new technique and as such there are currently few reports that have used PDF to analyse FTS catalysts. In work by du Plessis *et al.* PDF was used to follow the reduction of a Co/Al_2O_3 catalyst *in situ*, the PDF can be seen in figure 3. In particular a refinement of the data was performed to determine all cobalt phases present in the catalyst.

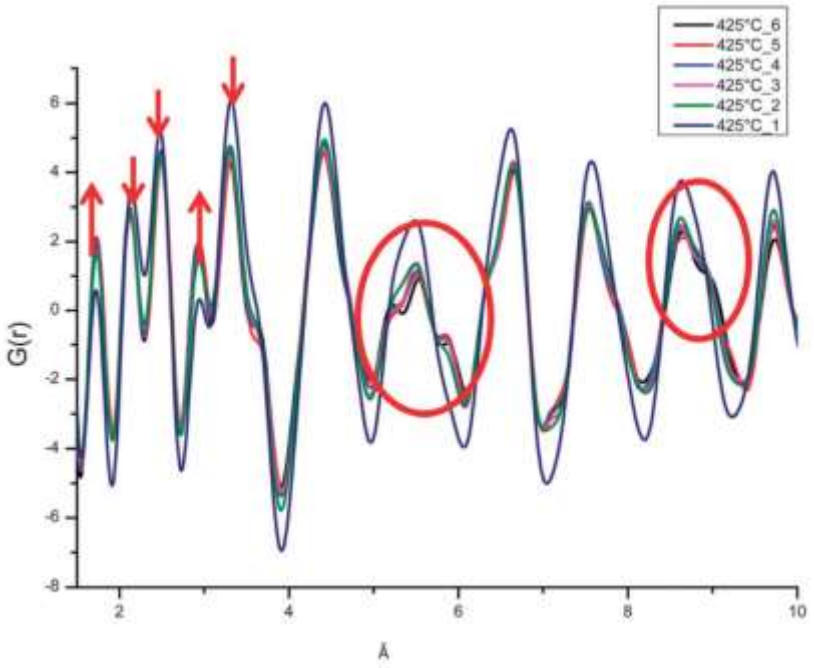

Figure 3: PDFs acquired during the reduction of Co/Al_2O_3. The temperature was held at 425 °C for 2 h. The numbers 1-6 in the figure legend correspond to consecutive 20 min diffractograms over the 2 h reduction period. Reproduced with permission from the Royal Society of Chemistry, du Plessis et al. Phys. Chem. Chem. Phys. 15 (2013) 11640–5[47].

The first five peaks that correspond to the short-range order are indicated in figure 3 by red arrows, and are observed to increase or decrease during the course of catalyst reduction. Table 2 shows the possible combinations of atomic pairs/interatomic distances that could give rise to these contributions in Figure 3. The key observation in this study is that 32 % of the cobalt in the sample is undetectable by XRD but which is observable using PDF. The relative abundances of different phases present in the catalyst calculated using both Rietveld refinement and PDF are compared in table 3.

Table 2: Summary of interatomic distances assigned, information extracted from reference [47].

Inter-Atomic Distance (Å)	Scattering pairs assigned to distances
1.7	Al-Al(γ-Al_2O_3), O-Al($Co_xAl_yO_2$), O-Co ($Co_xAl_yO_2$)
2.2	Al-O(γ-Al_2O_3)
2.5	Co-Co(Co_{fcc} and Co_{hcp})
3.1	Al-Al(γ-Al_2O_3), Al-Al(θ-Al_2O_3), Al-O(θ-Al_2O_3)
~3.5	Not assigned

More specifically the results show that PDF analysis determined a Co loading of 22 wt% (confirmed by ICP-OES, 21 wt%) [47]. However, from Rietveld refinement finds only 15 wt% (68 % of the cobalt present in the sample). Considering the aforementioned fact that not only the particle size, but the nature of the cobalt species is key to the activity of a FTS reaction, PDF enables the detection of species which are difficult to observe with conventional PXRD approaches– as the material is either not in crystalline form or the particles are too small to detect with XRD. The observation of such material is essential if the FTS is to be better understood and therefore this initial result highlights the potential of total scattering to the study of FTS catalysts.

Table 3: Relative abundances of material determined by PXRD and PDF. Information extracted from du Plessis *et al.* [47]. *Inductively Coupled Plasma Optical Emission Spectroscopy (ICP-OES) wet chemical analysis.

	Relative Abundance (wt%)		
	Rietveld	**PDF**	**ICP-OES***
Si	9	9	-
$Co_xAl_yO_4$	2	2	-
θ–Al_2O_3	19	24	-
γ–Al_2O_3	52	44	-
CoO	11	6	-
Co(fcc)	4	12	-
Co(hcp)	<1	3	-
Amorphous	3	-	-
Total wt% Co	***15***	***22***	***21***

One of the challenges in the interpretation of PDF data is that, due to the presence of scattering pairs from all components in the sample i.e. Co and Al-containing phases in this study, it is difficult to unambiguously assign a particular contribution to one specific component/phase. Thus for example, the contribution at 1.7 Å could be assigned to

tetrahedral Al^{3+}-O contributions typical of the support or else possibly, although unlikely, tetrahedral Co^{3+}-O species typical of an inverse spinel structure [48]. Notably however the lack of a significant positive component in the G(r) at ~ 1.9 Å suggests the absence of significant amounts of tetrahedral Co^{2+} containing spinel $CoAl_2O_4$ [49].

II.3. Small Angle X-Ray Scattering (SAXS)

SAXS is the detection of elastically scattered X-rays at very low angles, which are caused by long range inhomogeneities in the electron density of a sample, consequently the features probed by this technique are in the range of 1-100 nm [50]. This length scale results in the study of comparatively large scattering entities within the samples; structures such as the cobalt particles and pores within the supports. However, when characterising catalytic particles on porous supports, it is non-trivial to differentiate particles from pores using SAXS [51].

SAXS is mainly used to determine the morphology of particles/pores, this includes average size, size distribution, specific surface area and the shape of these structures, as well as the average distance between such features [52,53]. Synchrotron-based SAXS offers the opportunity to study such variations *in situ*, with extremely short collection times that facilitate real-time monitoring of catalysts under reaction conditions. SAXS is frequently performed simultaneously with conventional XRD (referred to as Wide Angle X-ray Scattering (WAXS) when combined with SAXS) as the different size ranges probed are complimentary [54]. SAXS measurements are independent of the crystallinity of the sample and so can be used to determine particle size, whereas, WAXS is able to determine crystallite size and the degree of crystallinity or phase purity.

Although SAXS generally provides morphological information, structural information concerning the surface of the cobalt particles can be obtained from this data providing insight into variations in the surface structure under reaction conditions [50]. In a recent study, Høydalsvik *et al.* used synchrotron-based SAXS to study Co-based FTS catalysts, providing an insight into the changes in the surface morphology of Co particles at the beginning of FTS, as well as a good description of relevant SAXS analysis for such catalysts [50]. The catalysts examined in the study were two Re promoted Co/γ-alumina catalyst (sample A and sample B), and SAXS measurements were taken during reduction and FTS, in a flow of H_2 and syngas respectively. WAXS was performed simultaneously to study the reduction of the cobalt oxide, the results of which were consistent with previous studies. ASAXS (Anomalous

Small Angle X-ray Scattering), a technique in which the X-ray energy is deliberately tuned near to a absorption edge to provide some element specificity in the features being probed, was performed independently on one sample to distinguish between Co particles and pores in the γ-alumina, resulting in a more meaningful discussion of the SAXS data [50].

The authors also used model *independent* analysis of the SAXS data and compared observations on the calculated values of the Porod exponent (α) and the scattering invariant (G*) (both explained in the following text) from the SAXS data in order to try and identify changes in morphology or shape of the Co particles during FTS and identify the most probable cause. The Porod exponent yields information concerning the surface of the particles. Whereas, the scattering invariant is dependent on the mean square fluctuation of electron density, a change in which would indicate a variation in density or mass of the particles [50]. The value for the Porod slope (α_0) is approximately 4 during reduction and increases to a value > 4 after the syngas is introduced, indicative of the change from a smooth 3D object to one with a continuous interface transition [50]; it is assumed that only the Co contributes to α_0, as the γ-alumina should be thermally stable at the temperatures used. It is therefore concluded that a change in cobalt shape or particle morphology occurs at the start of a FTS reaction. The key results from this paper are shown in figures 4 and 5, where the cyan regions represent the reduction process, and the red regions FTS.

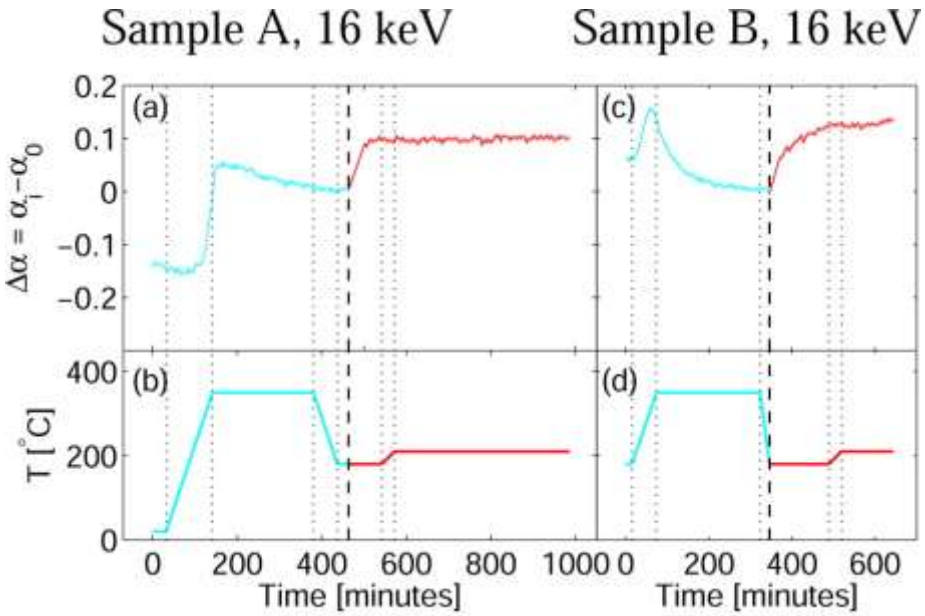

Figure 4: Variation in the Porod exponent and temperature over reduction and FTS. Reproduced with permission from the American Chemical Society, Høydalsvik et al. J. Phys. Chem. C. 118 (2014) 2399–2407 [50].

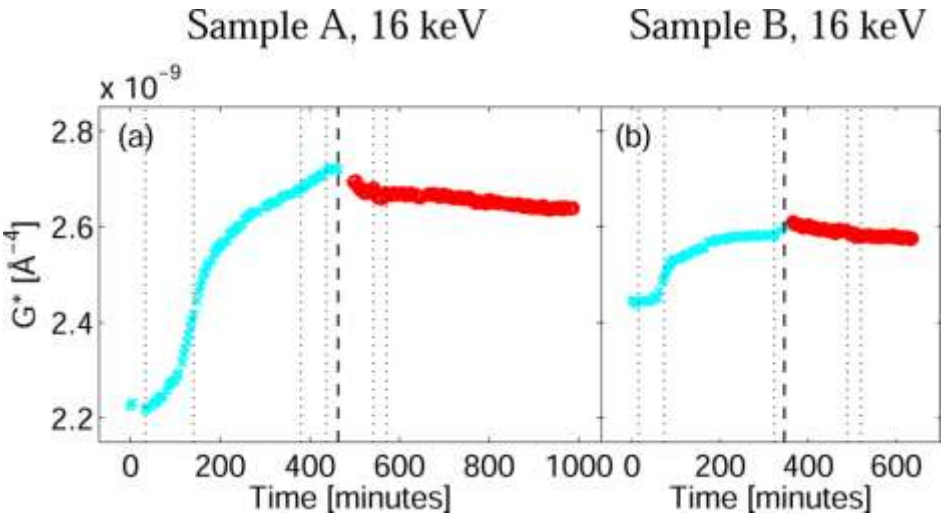

Figure 5: Variation in the scattering invariant (G*) over reduction and FTS. Reproduced with permission from the American Chemical Society, Høydalsvik et al. J. Phys. Chem. C. 118 (2014) 2399–2407 [50].

During reduction the scattering invariant increased significantly, this corresponds to reduction towards a cobalt metallic species, as Co^0 has a higher scattering density than Co_3O_4. As the syngas is introduced at the start of FTS there is a large increase in the Porod exponent for both samples, whereas, the invariant only reduces slightly with time on stream. Possible causes for the observed changes were proposed as follows (figure 6):

i) Shape change/faceting

ii) Surface reconstruction and relaxation

iii) Formation of a subsurface carbon layer

iv) Surface reoxidation

v) Adsorbed monolayer of CO/layer of hydrocarbons

vi) Diffusion or interactions with alumina support

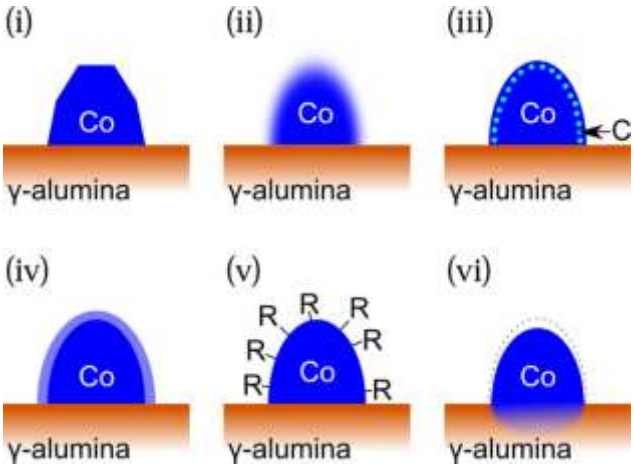

Figure 6: Schematic representations of the possible cobalt particle changes during FTS which could explain the observed data changes in the SAXS data: (i) faceting, (ii) surface reconstruction and relaxation, (iii) formation of a subsurface carbon layer, (iv) surface reoxidation, (v) adsorbed monolayer of CO or a layer of hydrocarbons, and (vi) diffusion/interaction with the alumina support. Reproduced with permission from the American Chemical Society, Høydalsvik et al. J. Phys. Chem. C. 118 (2014) 2399–2407 [50].

It was concluded that the most likely interpretation of the SAXS data is the migration of Co surface atoms caused by absorption of CO resulting in less well-defined particles.

III. Spectroscopic Techniques as applied to Co-based FTS catalysts

Cobalt-based catalysts are known to possess a variety of coordination and oxidation states and hence spectroscopic techniques are well suited for their characterisation. The elucidation of cobalt's different coordination environments and oxidation states permits the discovery of possible routes for optimising the cobalt-based catalysts' structures and thus performance. XAFS and X-ray photoelectron spectroscopy (XPS) techniques are particularly pertinent for this purpose as they are element specific and directly interrogate the local geometry, co-ordination and oxidation state of cobalt.

Cobalt has the electron configuration [Ar] $3d^7$ $4s^2$ and the most commonly found oxidation states are 0, +2, +3 and +4. Co^{2+} (d^7) is cobalt's most common valence state, which can adopt high-spin octahedral (CoO nanocages) [55] and tetrahedral ($CoAl_2O_4$) coordination environments [4]. Co^{3+} (d^6) is also present in octahedral coordination ($LaCoO_3$) [56] but on rare occasions is also found in the tetrahedral coordination [57]. Co^{4+} (d^5) is less stable and only observed as an intermediate during catalysis, particularly in electrocatalytic water

splitting [58]. Cobalt can also exist in a mixed valence state within the same compound; for example, the tetrahedrally coordinated +2 and octahedrally coordinated +3 oxidation states of cobalt are both present in Co_3O_4 [5].

III.1. X-ray Photoelectron Spectroscopy

X-ray Photoelectron Spectroscopy (XPS) has been used to investigate Fischer-Tropsch catalysts for a considerable time, however, only effects of promoter deposition on metal crystals were investigated in the late seventies. Ott *et al.* worked on iron-ruthenium alloys [59] and Bonzel *et al.* published a series of publications on potassium promoted iron crystals which were compared to the promotion of supported metal catalysts by alkali metals used for methanation or FTS [60,61]. Thanks to XPS, they were able to obtain quantitative information on the decomposition and desorption of CO on Fe(110) + K and clean Fe(110) but also on carbon deposition during FTS. Unfortunately, these model systems have their limitations compared to supported catalysts (interaction metal/support). Fleisch *et al.* continued Ott's study and were one of the first groups to investigate supported FTS catalysts with XPS. They studied Fe-Ru alloys on SiO_2 and noticed a slower coke deposition on this supported catalyst, indicated by the growth in intensity of the carbon C1s peak compared to the unsupported alloy powders.

Shortly afterwards, Meyers *et al.* started to use XPS for gaining understanding of cobalt based FTS catalysts [62]. XPS allowed them to highlight the presence of reduced cobalt species in addition to Co(II) on a decarbonylated and spent catalysts. Ever since, XPS has been used to detect the oxidative evolution of cobalt species following reduction and FTS reactions. The 2p transitions of Co are measured in order to carry out this characterization and the assignment of cobalt oxidation states is most readily accomplished by examination of the satellite structure of the $2p_{3/2}$ level and also by consideration of the spin-orbital splitting of the 2p levels. Co_3O_4 consists of octahedrally coordinated Co^{3+} and tetrahedrally coordinated Co^{2+}. A peak around 778 eV is characteristic of metallic Co [63]. On ionization, the 2p levels are split into $2p_{3/2}$ and $2p_{1/2}$ as a result of spin-orbit coupling. A $2p_{3/2}$ XPS peak found around 782 eV "with an intense shoulder at about 787-788 eV" denotes the presence of Co^{2+}[63]. However, for Co^{3+} species, the $2p_{3/2}$ peak shifts to lower energy and the shoulder becomes less intense. The $2_{p1/2}$ is around 15 eV greater than that of the $2p_{3/2}$ peak in both cases with the characteristic 1:2 intensity ratio relative to the $2_{p3/2}$. During calcination of Co^{2+}

species, the intensity of the $2p_{3/2}$ decreases and shifts to a lower energy, marking the conversion of Co^{2+} to Co^{3+} [63].

Another interesting feature of XPS is the possibility to determine particle sizes assuming both uniform distribution of particles in catalyst grains and high specific surface area (>100 m^2/g) of the support. For example, Khodakov *et al.* applied this method to cobalt Co_3O_4 particles on a SiO_2 support [64]. A simplified Kerkhof–Moulijn formula [65] can be applied to calculate the sizes of Co_3O_4 particles:

$$\left(\frac{I_{\mathrm{Co}}}{I_{\mathrm{Si}}}\right)_{\mathrm{exp}} = \left(\frac{I_{\mathrm{Co}}}{I_{\mathrm{Si}}}\right)_{\mathrm{monolayer}} \frac{1-\exp\left(-\frac{d}{\lambda_{pp}}\right)}{\frac{d}{\lambda_{pp}}}, \quad (6)$$

where $(I_{Co}/I_{Si})_{exp}$ is the experimental electron intensity ratio for Co 2p and the support (here Si 2p) peaks, d is the Co_3O_4 particle size, λ_{pp} is the inelastic mean free path (IMFP) of the Co 2p photoelectron passing through Co_3O_4 supported phase calculated using Seah and Dench's formula [66], $(I_{Co}/I_{Si})_{monolayer}$ is the predicted electron intensity ratio for Co 2p and Si 2p bands assuming monolayer coverage of silica by Co_3O_4 phase. $(I_{Co}/I_{Si})_{monolayer}$ is obtained according to equation (6) and photoelectron cross section values (σ_{Si}, σ_{Co}) from Scofield [67]:

$$\left(\frac{I_{\mathrm{Co}}}{I_{\mathrm{Si}}}\right)_{\mathrm{monolayer}} = \left(\frac{n_{\mathrm{Co}}}{n_{\mathrm{Si}}}\right)_{\mathrm{bulk}} \frac{\sigma_{\mathrm{Co}}}{\sigma_{\mathrm{Si}}} \left(\frac{E_k^{\mathrm{Co}}}{E_k^{\mathrm{Si}}}\right)^{-0.23}, \quad (7)$$

where $(n_{Co}/n_{Si})_{bulk}$ is the ratio of bulk atomic concentrations of Co and Si atoms, E_k^{Co} and E_k^{Si} are the kinetic energies of Co $2p_{3/2}$ and Si 2p electrons, respectively. Equation (7) shows that for a given $(n_{Co}/n_{Si})_{bulk}$, $(I_{Co}/I_{Si})_{exp}$ ratio increases with decreasing particle sizes, $(I_{Co}/I_{Si})_{exp}$ ratio close to $(I_{Co}/I_{Si})_{monolayer}$ indicates monolayer coverage of the support by cobalt atoms. However, Khodakov *et al.* observed particle sizes considerably smaller than the one calculated from XRD using the Scherrer equation. This difference has already been reported [68] and seems to be related to the limitations of XPS and XRD methods. The assumption of a uniform distribution of the supported phase between the bulk and outer surface of catalyst grains may be different from the reality of a calcined catalyst and the Kerkhof and Moulijn model might not always be suited for this method.

In modern times, XPS has become a very common technique in the field of catalysis but, despite its many benefits for the understanding of catalytic systems, some limitations apply. Because XPS is a surface technique, there is a limited amount of bulk information

XPS can provide, which may either be an advantage in understand surface processes or an impediment in studies of 3D porous materials. For some time "high pressure XPS" has existed in which samples are transferred between a high pressure cell and a vacuum environment and this has been used to good effect in studying particle size effects in cobalt catalysed FTS, [14] samples must still be stable in the vacuum environment.

More recently Near Ambient Pressure (NAP-) XPS has been developed significantly, due in large part to the higher flux and advantages of being able to tune the incident photon energy (and therefore limit the kinetic energy and consequent escape depth of electrons from within the sample), permitting depth profiling. The general development of synchrotron NAP-XPS is well described elsewhere [69], however the key point is it enables the acquisition of XP spectra in the 0.1 – 10 torr range; as noted previously the significance of this to catalysis is it provides ~ 10^6 collisions of gas molecules per second per surface atom of the sample and so makes mass transfer of adsorbates in the gas phase cease to be rate limiting in most cases [70]. In 2011 NAP-XPS was applied to study the redox behaviour of two Co nanoparticle systems pertinent to FTS (both in conjunction with XANES (X-ray Absorption Near-Edge Structure) measurements as discussed below). Use of the BESSY synchrotron allowed a detailed study of small (3.5 nm) cobalt nanoparticles as compared to Co(0001) single crystals in which the very different oxidation and reduction behaviour could be seen using the Co 2p edge, in particular the satellite structure in small pressures of oxygen is indicative of Co^{2+} in the nanoparticles, which is different to the bulk mixed oxide Co_3O_4 formed on the singly crystal [71]. The implications for the preparation and reduction of FTS catalysts are discussed. In the same year, studies of Pt-Co bimetallic nanoparticles using NAP-XPS were used to better understand possible promotional effects of precious metals (in this case Pt) in FTS. The Pt 4f signal was monitored for bimetallic 1:1 Pt:Co size controlled nanoparticles in a reducing atmosphere (0.1 mbar H_2), which allowed depth profiling of the elemental composition of the bimetallic nanoparticles, indicating surface segregation of a Pt shell around the surface (an observation confirmed by *in situ* TEM of a single particle under 0.1 mbar H_2) [72]. This is important in the context of FTS, where Pt is known to act as a promotor, as it argued that the "bimetallic metal particle" is the wrong model for understanding promotion as the Pt is seen to have a deleterious effect on reactivity in the analogous CO_2/H_2 reaction.

III.2. X-ray Absorption Spectroscopy

X-ray Absorption Spectroscopy or X-ray Absorption Fine Structure (XAS/XAFS) comprises both XANES, also known as Near Edge XAFS (NEXAFS), and Extended X-ray Absorption Fine Structure (EXAFS) spectroscopies [73]. Traditionally XANES has been used as a fingerprint technique providing information about both the electronic state and local geometry of cobalt, whilst EXAFS allows the determination of bond lengths and the coordination numbers of cobalt species under standard and *in situ* conditions to be obtained, without the need of long range ordering [74].

A key advantage of XAFS techniques is found in studies of oxidation state, that is it is element specific – especially for complex catalysts which contain a number of components this affords a substantive advantage in tracking the oxidation state of one part of the sample against techniques in which the oxidation or reduction must be inferred from the adsorption of desorption of gas molecules to/from the sample as a whole (e.g. temperature programmed reduction). [75]

In FTS catalysts, typically cobalt oxide in the form of the spinel Co_3O_4 is found in calcined catalysts immediately before activation in a reducing gas stream in preparation for FTS [76]. In this step Co_3O_4 is reduced to CoO and then to metallic fcc Co. Thus, it proceeds by this "two-step reduction": $[Co^{2+}][Co^{3+}] \rightarrow Co^{2+} \rightarrow Co^{0}$. As such the reduction can be monitored using XANES, an example of which is displayed in Figure 7.

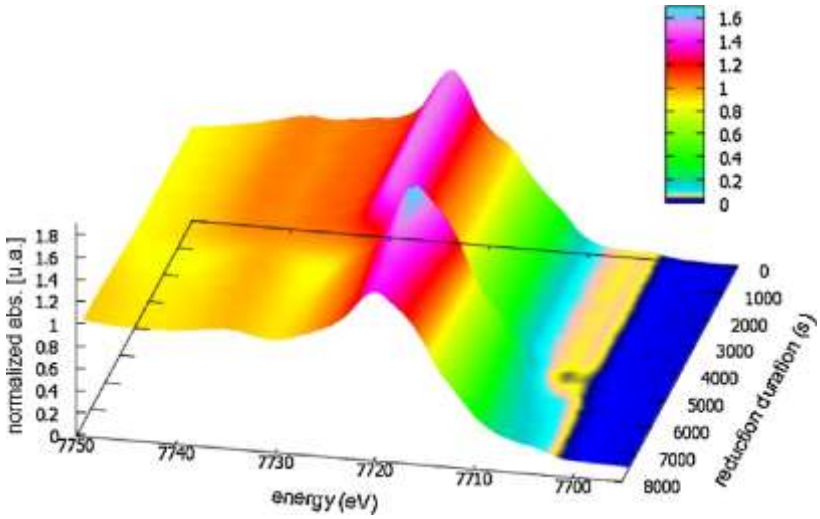

Figure 7: Time-resolved XANES spectra corresponding to the reduction of a Co/Al_2O_3 catalyst (7 wt%) in a flow of H_2 heated from RT to 400 °C with a ramp rate of 5 °C/min. Reproduced with permission from Elsevier, Rochet et al. Catal. Today. 171 (2011) 186–191 [76].

Figure 7 is a continuum of XANES spectra recorded over the course of an *in situ* reduction. [76] As the reduction time increases a distinct edge shift is observed from approximately 7725 to 7722 eV as well as an increase in the intensity of the rising edge, followed by a reduction in intensity consistent with a reduction to CoO then Co^0. Such characteristic changes in XANES features are often used to monitor *in situ* reductions of such catalysts.

Another situation in which it is useful to monitor oxidation state is in studying the possibility that water formed during the reaction is a source of deactivation. Here, albeit at low pressure (0.4 mbar), studies of a $Co/SiO_2/Si(100)$ model catalyst using Co K-edge XAFS showed that, even with $H_2O:H_2$ ratios of 1:1, the catalyst once reduced showed no evidence for oxidation occurring from 150 – 450 °C [9].

Furthermore, Co K-edge data has also been used to improve understanding of the impact of precious metal promotors on maintaining cobalt in a reduced state during the reaction. Precious metals, such as Pt, are currently added to industrial catalysts, but the role of the precious metal has been an ongoing source of debate. To help understand this effect (which increasingly appears to be attributable to the improved reduction of Co in the present of precious metals), a study contrasting the effects of Pt promotion on Co catalysts used Co Kedge data to follow the oxidation state of the cobalt component as a function of various reduction procedures, showing the more facile reduction of cobalt in the promoted case [77].

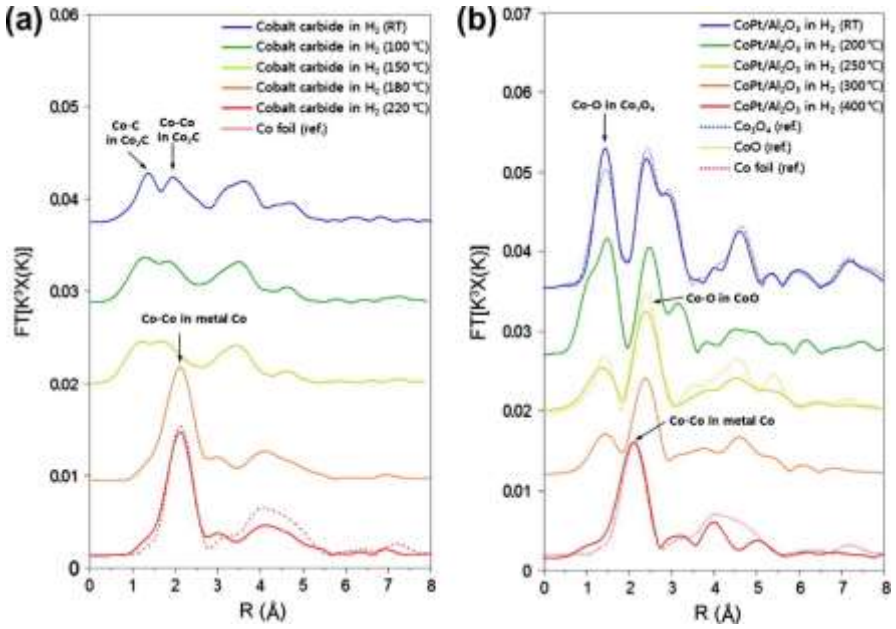

Figure 8: k^3-weighted Fourier-Transform magnitudes of Co K-Edge EXAFS spectra of the reduction in H_2 of a) Co_2C and b) $CoPt/Al_2O_3$. Reproduced with permission from Elsevier, Kwak et al. J. Catal. 307 (2013) 27–36 [78].

The ability to differentiate between fcc and hcp Co using XAFS is limited as the Co-Co interatomic distances and coordination numbers are identical for each polymorph. However, other features in the (E)XAFS spectra can be indicative of the structure. For instance an *in situ* XAFS study by Kwak *et al.* of the reduction of Co_2C and $CoPt/Al_2O_3$ catalysts, the 3rd and 4th peaks in the Fourier transformed EXAFS spectra (Figure 8) were used to indicate the structure [78]. The transformed EXAFS spectra of the Co^0 reduced from Co_2C (Figure 8a) possess a low amplitude 3rd peak and no 4th peak corresponding to the 4th coordination shell suggesting the Co^0 is hcp [79].

Carbon formed in FTS under hydrogen deficient conditions by the Boudouard reaction (equation 4) or via CO dissociation may interact with the cobalt-based catalyst, [80] affecting CO conversion and selectivity by forming cobalt carbide (Co_2C) [81]. Although Co is thought to be in the +2 oxidation state in Co_2C, the carbide exhibits strong metallic properties (similar to most transition metal carbides) and therefore can be considered to be an hcp lattice with C incorporated at interstitial sites [81]. Co_2C can also be formed by the carburization of Co_3O_4 as shown in equation 5.

Boudouard reaction [4]: (4)

$2CO \rightarrow CO_2 + C$

Carburization of Co_3O_4 [81]: (5)

(1) $Co_3O_4 + CO \rightarrow 3CoO + CO_2$

(2) $2CoO + 4CO \rightarrow Co_2C + 3CO_2$

Metallic cobalt catalysts in hcp form exhibit high activity, attributed to facilitating CO dissociative adsorption and thus also increasing the chain length of the hydrocarbons attained in LTFT. [78] An example of the use of EXAFS to identify Co_2C in cobalt based catalysts is a study by Mohandas *et al.*, which investigated the role of Co_2C in the hydrogenation of CO. [81] Unsupported Co_2C catalysts were synthesised by the carburisation of Co_3O_4. The presence of Co_2C was verified by XRD. *Ex situ* XAFS measurements were taken after carburisation and once the catalyst was spent (tested in a slurry phase reactor at P = 20 bar, H_2:CO = 2:1 and T = 493-523 K). The corresponding EXAFS are displayed in Figure 9 and the Fourier transform spectra for the carburized catalysts (with and without passivation) show Co-C (at 1.924 Å and 1.862 Å) and Co-Co (2.505 Å and 2.441 Å) in the first and second nearest neighbour shells, thus detecting the carbide present in the sample.

+

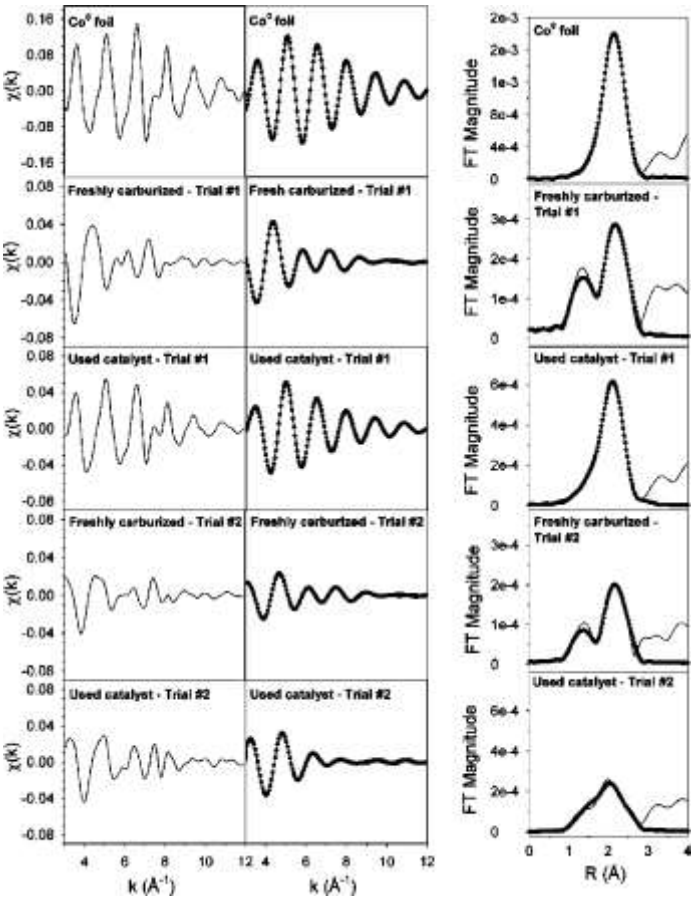

Figure 9: EXAFS and Fourier Transform magnitude spectra of a Co^0 reference, Co_2C catalyst once prepared and once spent, recorded at the Co K-edge. Reproduced with permission from the American Chemical Society, Mohandas et al. ACS Catal. 1 (2011) 1581–158 [81].

Cobalt aluminate ($CoAl_2O_4$) species are formed from the solid-state reaction between the alumina and the cobalt at the metal-support interface and are thought to mainly form under reducing conditions [4,82]. When investigating oxidation as a deactivation process, for Co/Al_2O_3 catalysts of 15 and 25 wt%, studied pseudo *in situ* after high H_2O/CO ratios (up to 25% H_2O) removed at various stages from a slurry FTS reactor, an increased tetrahedral environment of Co^{2+} clusters can be seen in the XANES spectra. This indicates the formation of $CoAl_2O_4$ over Co_3O_4, which is likely as this transformation is thermodynamically favourable [83] (see Figure 10).

By observing the XANES derivative spectra of the cobalt species found during FTS (figure 10), the change in oxidation state of cobalt species can be portrayed by observing the shift of the peaks (with the aid of the line drawn through the centre of the tallest peak in spectrum g). [84] The Co K-edge peak of the Co_3O_4 and $CoAl_2O_4$, which is located around 7717 eV, is characteristic of Co^{2+} [80]. This increasing intensity of the Co^{2+} pre-edge peak in the spectra indicates the absence of a centrosymmetrical structure [85]. Thus, the Co^{2+} is in a tetrahedral environment as opposed to an octahedral environment, which has a centre of inversion. Conversely, the reduced peak that is shifted to a higher energy (around 7722 eV) conveys the presence of Co^{3+} in an octahedral coordination.

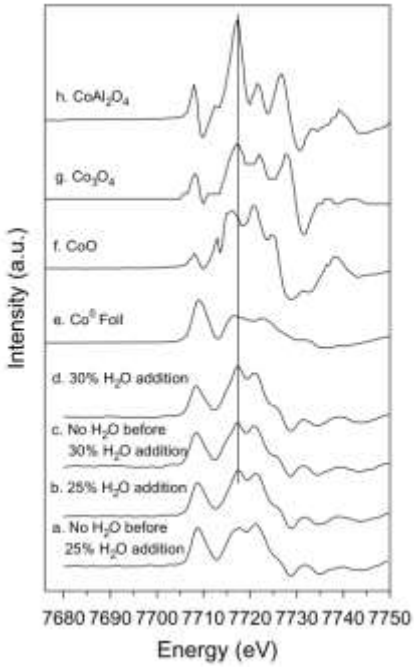

Figure 10: XANES first derivative spectra of cobalt species present during FTS synthesis a) after stabilisation of FTS, b) after the addition of 25 % H_2O, c) after a period of recovery, d) after addition of 30 % H_2O, e-h) reference foils/compounds. For a Co/Al_2O_3 25 wt% catalyst. Reproduced with permission from the Elsevier, Jacobs et al. Appl. Catal. A Gen. 270 (2004) 65–76 [84].

III.3. Soft XAFS

XAFS can also be performed using soft X-rays from a synchrotron source (X-rays of energies less than 5 keV). Although significantly less penetrating than hard X-rays, soft X-ray energies in the range of 200 – 4000 eV allow for the examination of the K-edges of 'ligand elements' such as C, O, S and Cl. Which are able to act as 'reporter' elements for metal sites determining the electronic state of the ligand and its metal complex [86], or in the case of FTS may themselves be present in adsorbed species on the catalyst (C or O K-edges fall in this region). Additionally, soft X-rays allow for the probing of Co L-edges, which are typically more sensitive to Co oxidation and coordination state.

Co/TiO_2 and $Co/Mn/TiO_2$ FTS catalysts were studied using a differential pumping method similar to that described above for NAP-XPS and the extent of Co reduction identified as an important parameter as a result of monitoring the evolution of Co oxidation state based upon it L-edge spectra [87].

As soft X-rays are readily absorbed by most gases over relatively short length scales (mm), *in situ* measurements have relied upon probing samples placed close to a X-ray transparent window, which is able to hold pressure on one side with vacuum on the other, an example of which is given in Figure 11. For this purpose silicon nitride membrane windows have been employed and Co-L edge spectra have been reported up to several atmospheres using this technique [88]. Spectra are then acquired using the total electron yield method in which a drain current is measured between electrical ground and the sample (resulting from ejected electrons, and secondary electron emission from the sample).

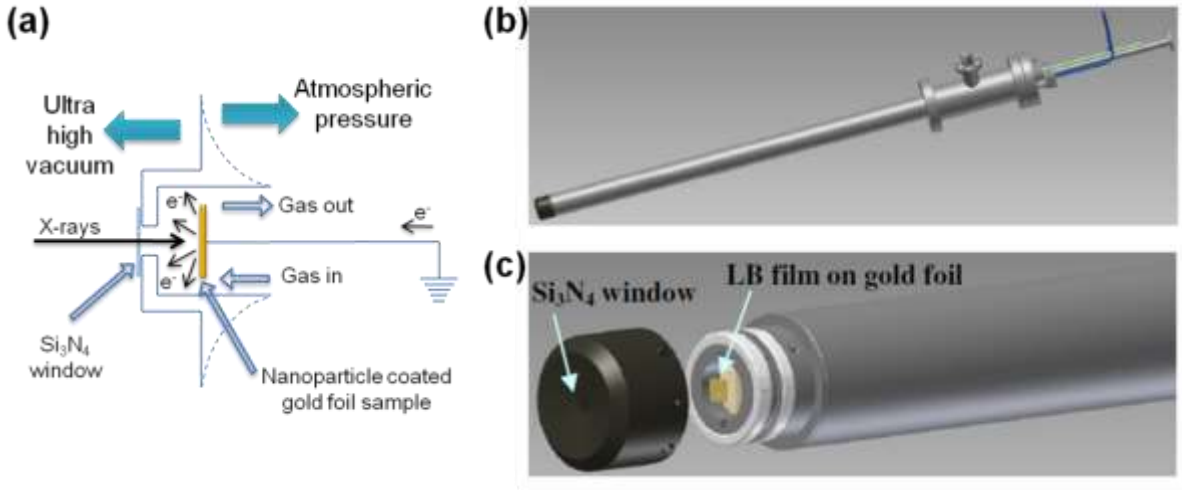

Figure 11: a) Schematic of *in situ* soft XAFS cell showing gas flow and b, c) 3D visualisation of the cell and sample holder. Reproduced with permission from Wiley-VCH, Somorjai et al. Angew. Chem. Int. Ed. 50 (2011) 10116–29 [89].

This method was adopted for studying model Co FTS catalysts at higher pressures by Salmeron *et al.* in 2009 [90]. They were able to follow the reduction in hydrogen flow at 1 bar of 3 and 10 nm (average sized) nanoparticles using the Co L-edge by this technique, starting in both cases with octahedrally co-ordinated CoO, and observing the formation of metallic cobalt. Notably they identify in addition to the more realistic pressure, the choice of using nanoparticle models of improved size control allows them to address questions about particle size effects, not addressed in previous studies using incipient wetness catalysts. The same group more recently studied CO dissociation on similar cobalt nanoparticle based FTS catalysts [91]. XAFS measurements were taken at both the O K-edge at 543.1 eV and the Co L_2-edge and L_3-edge at 793.2 eV and 778.1 eV respectively during various stages of the experiment. The samples were in the form of cobalt nano-particles (of sizes of 4, 10 and 15

nm) deposited on gold foil, which was held within a cell with a nitride window approximately 100 nm thick. The samples were heated using an IR laser and the reactive gas was passed though the cell at a flow rate of 40ml/min.

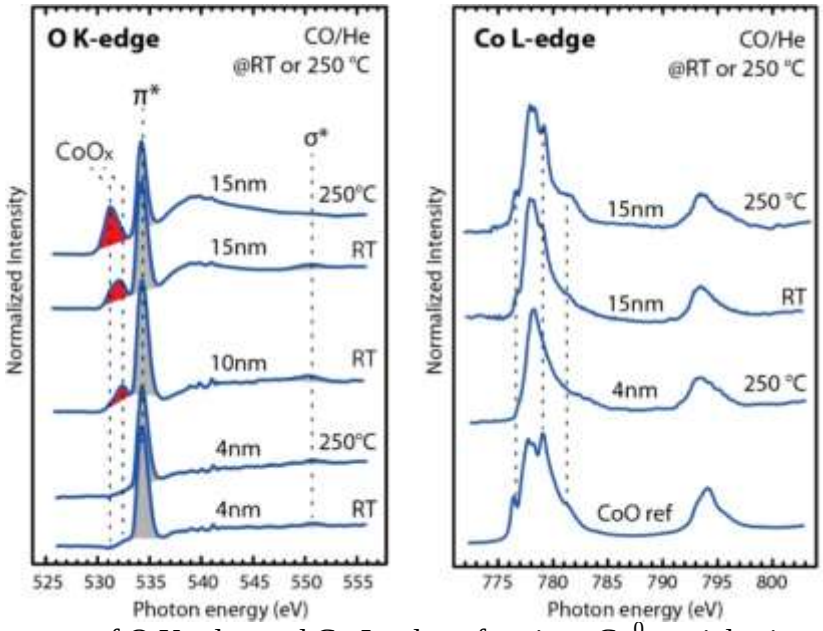

Figure 12: XAFS spectra of O K-edge and Co L-edge of various Co^0 particle sizes and reaction temperatures. Reproduced with permission from the American Chemical Society, Tuxen et al. J. Am. Chem. Soc. 135 (2013) 2273–8 [91].

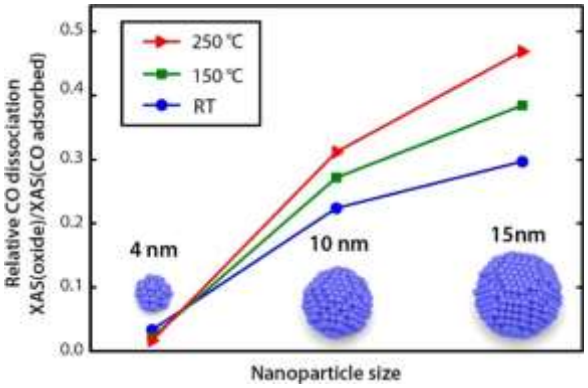

Figure 13: Calculated variations in relative CO dissociation for particle sizes of 4, 10 and 15 nm, at temperatures of RT, 150°C and 250°C. Reproduced with permission from the American Chemical Society, Tuxen et al. J. Am. Chem. Soc. 135 (2013) 2273–8 [91].

The XAFS measurements of 4, 10, and 15 nm cobalt nano-particles were taken after 5 min in a flow of CO/He (1:1) at 250 °C or room temperature are shown in figure 12. The O K-edge spectra show an intense π* peak at 534.2 eV and a weak σ* peak at 550 eV, consistent with the absorption of CO on cobalt. Another peak at ~531 eV which was attributed to CoO_x was observed in some of the spectra, the breadth of the peak indicates the potential presence of mixed cobalt oxides. Subsequently, this is also supported by the detection of CoO peaks in the corresponding Co L-edge spectra (figure 11). The CoO_x peak in the O K-edge spectra was attributed to the emergence of surface oxides on the nanoparticles indicating a sizeable proportion of CO molecules had (directly or indirectly) undergone dissociative absorption. The peak is barely detectable in the 4 nm sample, clearly observed in the 10 nm, and most prominent in the 15 nm sample. This indicated a size dependence of CO dissociation as well as a temperature dependence. The size dependence is illustrated more clearly when the sizes of nano-particles are plotted against the ratio between the integrals of the CoO_x peaks and the π* peaks, providing an approximate measure of the tendency of CO to dissociate. Some caution must be exercised in the wider implications for FTS, however, as the results obtained use gold as a support (rather than a more conventional oxide) and the nanoparticles used are reported to be prepared via a synthetic route employing triphenylphosphine oxide [92], a potential FTS poison [93]. Nevertheless it represents an interesting demonstration of using soft X-ray XAFS to probe cobalt nanoparticles reacting with the FTS reactant CO. Additionally it shows the capacity of soft X-rays to monitor low atomic number elements, typical of those originating from the adsorbate, such as oxygen in CO, or dissociated onto the cobalt surface.

Tuxen *et al.* also performed measurements on the 4 nm nano-particles during a repeated run of the treatment described above, in a flow of CO/He then pure He, however that was then followed by a pure H_2 step. All steps were also performed at temperatures of: 20°C, 150°C and 250°C. For the initial repeated stages the results are consistent with earlier experiments on the 4 nm particles, with an absence of a CoO_x peak and low CO absorption. However, once the H_2 was added a clearly observable CoO_x peak emerged in the O K-edge spectra (figure 14a), the evolution of the intensities of these peaks can be seen in figure 14c. These results indicate a size dependence of the nanoparticles for CO dissociation, and that that CO dissociation occurs more rapidly in the presence of H_2. However, the apparent activation energy for the process resulting in the loss of the π* peak shown in Figure 13 is given as 24 kJ mol^{-1} – this is not only much less than typical apparent activation energies for FTS in general (~100 kJ mol^{-1}), [94] but significantly less than even the lowest calculated energy barriers for H-assisted pathways on corrugated surfaces (~ 43 kJ mol^{-1}) [95]. In combination with the cautions raised above this suggests further work is needed to understand the relevance of these results to practical FTS catalysts.

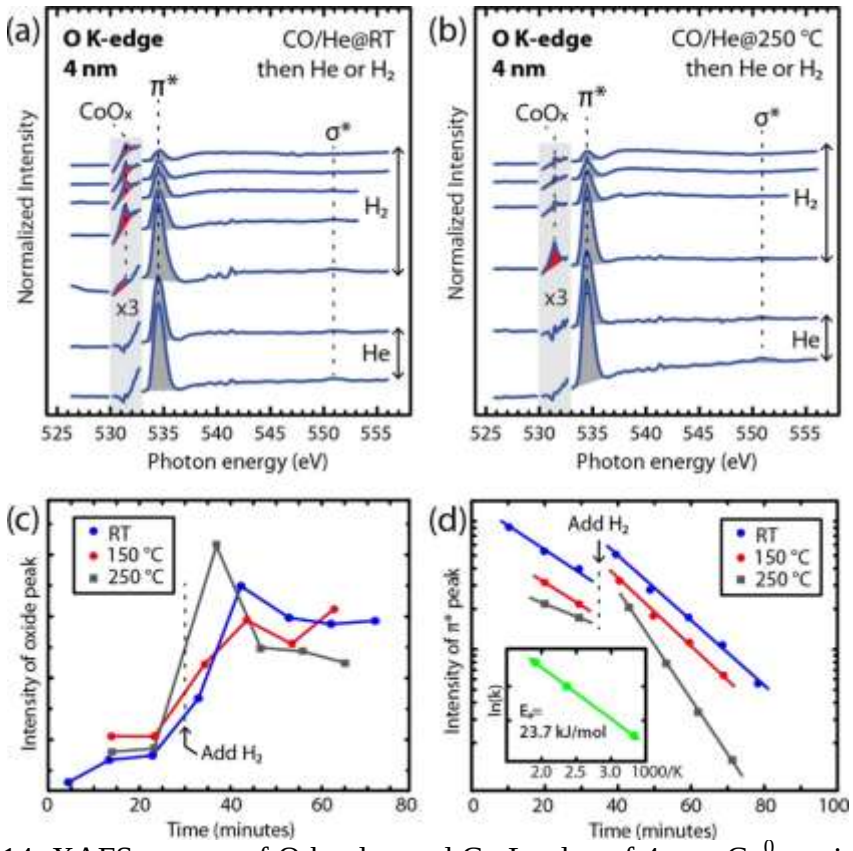

Figure 14: XAFS spectra of O k-edge and Co L-edge of 4 mm Co^0 particle sizes at a) room temperature and b) 250 °C and graphs displaying how the intensity of the c) CoOx and d) π* peaks vary with treatment time run at various temperatures (note logarithmic y-axis in

d; the inset in d shows the apparent E_a for the process changing the π^* peak intensity in the region after H_2 addition. Reproduced with permission from the American Chemical Society, Tuxen et al. J. Am. Chem. Soc. 135 (2013) 2273–8 [91].

Soft X-ray XAFS has also been used to investigate the possible promotional effects of Pt (discussed above as important for the mechanism of FT and possible reducibility of cobalt oxide). Co and CoPt nanoparticles were first studied in oxidising environments – the Pt being shown to enhance both reducibility and oxidation [96]. The Co L-edge spectra were analysed using a least squares fit to a linear combination of reference spectra for cobalt in different oxidation states and environments (e.g. tetrahedral vs octahedral). Although it can be shown that CoPt bimetallic nanoparticles achieve improved reducibility of the Co (as demonstrated by soft X-ray XANES [72,96], the NAP-XPS results discussed above showed this to be a poor model for an actual catalyst as a result of Pt surface segregation. The same group therefore also employed Co-L edge spectroscopy to study the effect of H_2 spillover between Pt and Co nanoparticles prepared separately and co-deposited onto a silicon wafer. During *in situ* reduction experiments, in all case the Pt nanoparticles were found to significantly increase the extent of reduction of the adjacent cobalt nanoparticles – suggesting H_2 migration is implicated in the mechanism by which platinum promotes the activity of cobalt in these types of catalyst [97].

More recently, Co-type FT catalysts using TiO_2 as a support have been compared to SiO_2 supported catalysts, again using soft X-ray Co L-edge spectroscopy to monitor oxidation state. An interesting redox behaviour has been observed in which for Co/TiO_2, partially oxidised Co appears more active. This remains to be fully understood, but is thought to be due in part to the interfacial CoO/TiO_2 sites present in the materials and to the TiO_2 decorating (and blocking reactant access to) some of the Co surface area in the fully reduced material obtained only at higher temperatures where oxide migration also occurs [98].] Again the ability to follow the oxidation state of a specific component of the material is invaluable. Interestingly in this same work the speciation of carbon on the surface was also monitored during CO_2 hydrogenation and provides evidence mostly of carbon bonded to hydrogen or oxygen on the surface, with no evidence for any carbide formation.

III.4. Transmission X-Ray Microscopy

Transmission X-ray Microscopy (TXM) using synchrotron radiation was originally performed on Co catalysts by Cats *et al.* [99]. The catalysts studied were Co/TiO_2 of 10 wt% and 15 wt% cobalt, examined during reduction in a flow of H_2 and FTS under conditions of T = 523K, P = 10 bar and $H_2/CO = 2$. TXM was used to obtain 2D chemical maps, XANES spectra were collected for each pixel by varying the beam energy, and the 3D elemental distribution of an individual particle was collected using acquisition tomography above and below an absorption edge [99].TXM and XANES were used to examine the change in chemical composition for the sample in terms of Co^0, CoO and $CoTiO_3$ on the local and long range length scales respectively. Both the 2D chemical maps produced by TXM and the composition obtained from analysis of the XANES spectra agree that before reduction the cobalt is in the form of Co_3O_4. After reduction the composition changes to mostly Co^0 with a statistically insignificant quantity of CoO and $CoTiO_3$ [99].

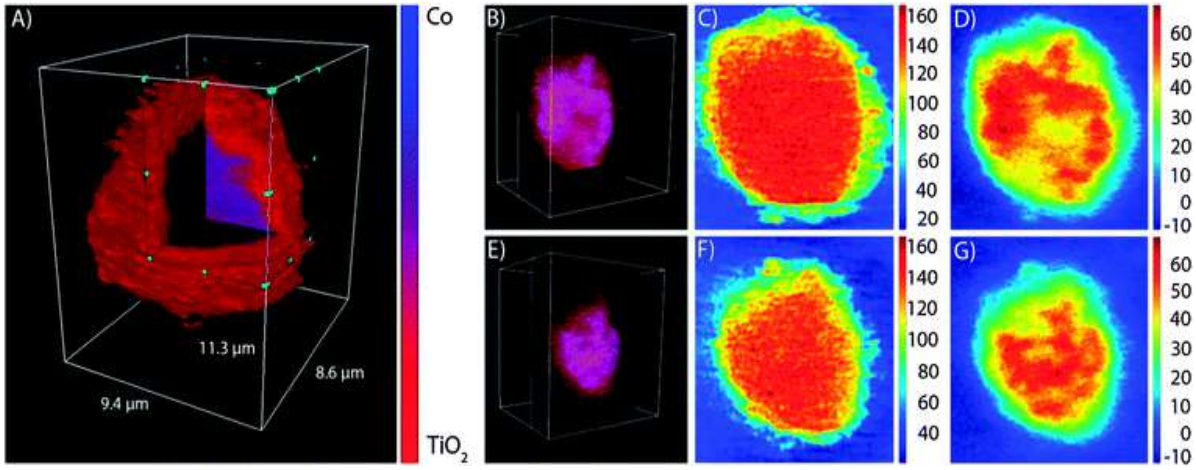

Figure 15: TXM images. A) 3D representation of an unreduced Co/TiO_2 particle measured at the Co K-edge. Red represents contributions from TiO_2 and blue represents contributions from cobalt. Images B-D and E-G show two slices though the particle. Reproduced with permission from the Royal Society of Chemistry, Cats et al. Chem. Commun. (2013) 4622–4 [99].

The 3D tomographic image of a catalyst particle of the unreduced 15 wt% Co/TiO_2 at the Co K-edge is seen in figure 12, as well as 2D slices of the image [99]. It can be seen that the cobalt in the sample is concentrated at the centre of the catalyst particle, and under standard FTS conditions, there is no re-oxidation of cobalt or a metal-support intermediate compound formation. However, considering the size of the nanoparticle (18 nm average as

determined by Scherrer analysis) and the spatial resolution of the beam (30 nm), the truly active nanoparticles – either metallic or mixed oxides – might not be observed. Previous studies have also shown that small Co_xO_y nanoparticles are extremely difficult to reduce, retaining their oxidic nature [100–103]. Since this study cannot include these small particles in the analysis, it would not be sensitive to their role in the FTS reaction.

An additional study by Cats *et al.* published recently used multiple microscopy techniques over several length scales (hard and soft X-ray TXM, as well as STEM-EELS) to study Co/TiO_2 catalysts. [104] Here it was observed that during FTS Co became redistributed on the microscale forming a layer around the TiO_2 particles. This result is notable as it appears contrary to the previously reported behaviour of Co on TiO_2 samples where Co was observed to become encapsulated by TiO_2, leading to FTS catalysts with lower activity. What is clear however is that both studies suggests an intimate contact between the TiO_2 and Co most likely driven by a strong metal support interaction (SMSI). [105,106]

IV. Conclusions and Outlook

The present review of X-ray scattering and spectroscopic methods demonstrates the key information that can be obtained on cobalt-based FTS catalysts which can help us to better understand the issues surrounding their activation and deactivation. It is likely that this new insight has been used to design/create better performing catalysts as a result. Despite this, there remain a number of issues that beset the technology which impact on its viability. Needless to say, we feel that there is a wealth of information on the nature and function of these catalysts that remains to be discovered, some of which will surely help in understanding the significance of some of the observations made in previous studies. Here we highlight some of the outstanding questions and consider how SR methods applied under *in situ*/*operando* conditions could be employed to generate a better understanding of these problems as well as providing a basis for potential solutions:

a) The occurrence and significance of Co oxide (re)-formation under reaction conditions.

Whilst conventional packed-bed studies have observed that Co reoxidation does occur under FTS conditions, more recent high-resolution X-ray nanospectroscopy suggested

otherwise. [99] Whilst the comment can be made that the latter only examines a single and rather large particle, the results from both studies could be affected by for example gas diffusion as well as the position of sample illumination along the length of the reactor bed which, if operated in plug-flow mode, leads to a change in gas composition along the reactor length. Future *in situ*/*operando* studies should therefore consider the impact of spatial variation on the results obtained when measuring under process conditions so as to be able to put the results obtained into a better context of catalytic activity in a reactor.

b) Determining the importance of hcp, fcc phases and hcp/fcc stacking faults on activity and selectivity.

Some key studies have illustrated an effect of particle size of what seems most likely to be fcc particles on Co FTS activity and product distribution although the effects of a combination of close-packing arrangement and particle size is still unknown. It appears however that there is a lower-limit in particle size for hcp-forms somewhere around 6 nm. [107] There is some consensus on hcp particles being more active than fcc ones although more recently the focus has shifted towards an evaluation of faulted fcc/hcp or faceted structures which may yet prove to be the nanoparticle of choice for even greater activity. An XRD/PDF study, particularly under process conditions would prove most revealing in this regard.

c) The role and properties of promoter elements on catalytic activity.

The role of promoters on the catalytic activity remains a long standing issue for Co FTS catalysts. It is clear that the addition of small quantities of noble metal improves catalytic activity and stability, ostensibly by improving the reducibility of Co, [108] and ensuring rapid dissociative chemisorption of H_2 that may prevent oxidation under the conditions of the reaction. Promoter optimisation must therefore be key to any future use of promoted FTS catalysts due to the expense of such metals. Understanding promotion may also facilitate the use of less precious metal or even replacement. The full extent of the effect of the presence of promoters on deactivation is not understood and that of the catalysts synthesis conditions (e.g. change in pH that arises from co-precipitation). A number of studies attempting to address this question have been presented, but further studies targeting these important areas would therefore be useful, particularly EXAFS studies.

d) The significance of diffraction-silent cobalt on catalytic activity and stability.

Diffraction-based studies have provided valuable observations on Co-based FTS catalysts as their Co loading is high, however much of the catalyst is in the form of diffraction silent material; diffraction silent Co has recently been shown to be approximetaly 30 % of total cobalt content. [47] XAFS has always provided useful information on the diffraction silent material, and will continue to play a key role in this, although it is limited to bulk material. Complementary, CT techniques offer the opportunity to observe diffraction silent material, albeit limited to single particles/small groups of particles and therefore vulnerable to statistical errors and misinterpretation. Researchers have already successfully demonstrated the effectiveness of techniques such as XRD-CT [109], PDF-CT [110], and XAFS-CT for the detection of previously unseen or amorphous phases. Therefore, a vital step into truly understanding FTS catalysts would be to undertake a multi-technique CT approach using SR radiation, whereby Co^0, CoO, Co_3O_4, Co_2C, and amorphous/nano-crystalline (with low crystallinity) Co can be detected. Thus the phase, valency and size/shape changes can be identified throughout FTS not only in relation to time on-stream, but also in terms of location inside typical reactor set-ups. In addition to this *in situ* PDF experiments could provide a wealth of information on the behaviour of *all* material in the sample, including that which is diffraction silent.

e) The effects that particle size has on all of the above.

Co particle size affects the overall activity of the catalyst by complex relationships with the factors discussed above. Any comprehensive understanding of FTS catalysts and the issues described above must also account for these effects. Studies must be conscious of particle size effects and, where possible make observations of changing particle/crystallite size in experiments by the use of XRD, SAXS and XAFS among other techniques.

f) Understanding surface restructuring/carbon deposition during initial activation and after longer reaction times.

Surface restructuring is too subtle a change to be detected well by bulk techniques, yet has a very tangible effect on the initial activity of the Co particles and may even contribute to the

deactivation of the catalysts in the longer term. [50] It is therefore necessary to use a broader range of techniques to fully understand these effects. The use of nanospectroscopy and TXM has proved effective in observing the spatial elemental composition under reaction conditions including the behaviour of the surface. [99] With the continued improvement of spatial and time resolution of nano/μ-sized beams future experiments will be capable of investigating catalyst particles of more realistic sizes in *operando*, such experiments will be able to provide insight into the special evolution of the catalyst particles specific to any surface reconstruction.

In addition, a study which uses GISAXS measurements of particles on 2D model catalysts could determine variation in particle shape, but also inter-particle distances and examine the facets. This would make use of the high targeting of particle size (if particle size distribution is tightly controlled) of microscopic techniques without the statistical errors inherent in such techniques.

V. Acknowledgements

The authors would like to thank DUBBLE (a collaborative effort between the Dutch and Flemish research councils – NWO/FWO) and the UCL M3S-CDT/EPSRC for funding for Jennifer J. Herbert, David J. Martin and Andrew M. Beale. BP is thanked for funding for Pierre Senecal, and the Durham University Addison Wheeler Fellowship and The Leverhulme Trust ECF schemes for supporting Simon K. Beaumont.

References

1 F. Trippe, M. Fröhling, F. Schultmann, R. Stahl and E. Henrich, *Fuel Process. Technol.*, 2011, **92**, 2169–2184.

2 D. Leckel, *Energy and Fuels*, 2009, **23**, 2342–2358.

3 M. E. Dry, *Catal. Today*, 2002, **71**, 227–241.

4 A. Y. Khodakov, W. Chu and P. Fongarland, *Chem. Rev.*, 2007, **107**, 1692–744.

5 N. Osakoo, R. Henkel, S. Loiha, F. Roessner and J. Wittayakun, *Appl. Catal. A Gen.*, 2013, **464-465**, 269–280.

6 R. Riva, H. Miessner, R. Vitali and G. Del Piero, *Appl. Catal. A Gen.*, 2000, **196**, 111–123.

7 D. Schanke, A. M. Hilmen, E. Bergene, K. Kinnari, E. Rytter, E. Ådnanes and A. Holmen, *Catal. Letters*, 1995, **34**, 269–284.

8 P. J. van Berge, J. van de Loosdrecht, S. Barradas and A. M. van der Kraan, *Catal. Today*, 2000, **58**, 321–334.

9 A. M. Saib, A. Borgna, J. van de Loosdrecht, P. J. van Berge and J. W. Niemantsverdriet, *J. Phys. Chem. B*, 2006, **110**, 8657–64.

10 A. Martinez and G. Prieto, *J. Catal.*, 2007, **245**, 470–476.

11 J. P. den Breejen, P. B. Radstake, G. L. Bezemer, J. H. Bitter, V. Frøseth, A. Holmen and K. P. de Jong, *J. Am. Chem. Soc.*, 2009, **131**, 7197–203.

12 R. Reuel, *J. Catal.*, 1984, **85**, 63–77.

13 G. Prieto, A. Martínez, P. Concepción and R. Moreno-Tost, *J. Catal.*, 2009, **266**, 129–144.

14 Z. Wang, S. Skiles, F. Yang, Z. Yan and D. W. Goodman, *Catal. Today*, 2012, **181**, 75–81.

15 S. D. M. Jacques, O. Leynaud, D. Strusevich, P. Stukas, P. Barnes, G. Sankar, M. Sheehy, M. G. O'Brien, A. Iglesias-Juez and A. M. Beale, *Catal. Today*, 2009, **145**, 204–212.

16 M. Behrens and R. Schlögl, in *Characterization of Solid Materials and Heterogeneous Catalysts*, Wiley-VCH Verlag GmbH & Co. KGaA, 2012, pp. 609–653.

17 K. H. Cats and B. M. Weckhuysen, *ChemCatChem*, 2016, n/a–n/a.

18 A. M. Saib, D. J. Moodley, I. M. Ciobîcă, M. M. Hauman, B. H. Sigwebela, C. J. Weststrate, J. W. Niemantsverdriet and J. van de Loosdrecht, *Catal. Today*, 2010, **154**, 271–282.

19 N. E. Tsakoumis, R. Dehghan-Niri, M. Rønning, J. C. Walmsley, Ø. Borg, E. Rytter and A. Holmen, *Appl. Catal. A Gen.*, 2014, **479**, 59–69.

20 S. Rane, Ø. Borg, E. Rytter and A. Holmen, *Appl. Catal. A Gen.*, 2012, **437-438**, 10–17.

21 W. Zhou, J.-G. Chen, K.-G. Fang and Y.-H. Sun, *Fuel Process. Technol.*, 2006, **87**, 609–616.

22 A. M. Beale, S. D. M. Jacques and B. M. Weckhuysen, *Chem. Soc. Rev.*, 2010, **39**, 4656–72.

23 J. D. Grunwaldt and C. G. Schroer, *Chem. Soc. Rev.*, 2010, **39**, 4741–53.

24 D. Grandjean, A. M. Beale, A. V Petukhov and B. M. Weckhuysen, *J. Am. Chem. Soc.*, 2005, **127**, 14454–65.

25 E. A. Owen and D. M. Jones, *Proc. Phys. Soc. Sect. B*, 1954, **67**, 456–466.

26 S. Sasaki, K. Fujino and Y. Takéuchi, *Proc. Japan Acad. Ser. B Phys. Biol. Sci.*, 1979, **55**, 43–48.

27 W. L. Roth, *J. Phys. Chem. Solids*, 1964, **25**, 1–10.

28 J. Clarke and K. H. Jack, *Chem. Ind.*, 1951, **46**, 1004–1005.

29 K. Toriumi, M. Ozima, M. Akaogi and Y. Saito, *Acta Crystallogr. Sect. B Struct. Crystallogr. Cryst. Chem.*, 1978, **34**, 1093–1096.

30 Ø. Borg, N. Hammer, S. Eri, O. A. Lindvåg, R. Myrstad, E. a. Blekkan, M. Rønning, E. Rytter and A. Holmen, *Catal. Today*, 2009, **142**, 70–77.

31 H. Karaca, O. V. Safonova, S. Chambrey, P. Fongarland, P. Roussel, A. Griboval-

Constant, M. Lacroix and A. Y. Khodakov, *J. Catal.*, 2011, **277**, 14–26.

32 W. Chu, P. Chernavskii, L. Gengembre, G. Pankina, P. Fongarland and A. Khodakov, *J. Catal.*, 2007, **252**, 215–230.

33 N. E. Tsakoumis, A. Voronov, M. Rønning, W. Van Beek, Ø. Borg, E. Rytter and A. Holmen, *J. Catal.*, 2012, **291**, 138–148.

34 M. Rønning, N. E. Tsakoumis, A. Voronov, R. E. Johnsen, P. Norby, W. van Beek, Ø. Borg, E. Rytter and A. Holmen, *Catal. Today*, 2010, **155**, 289–295.

35 W. van Beek, O. V. Safonova, G. Wiker and H. Emerich, *Phase Transitions*, 2011, **84**, 726–732.

36 S. Nikitenko, A. M. Beale, A. M. J. van der Eerden, S. D. M. Jacques, O. Leynaud, M. G. O'Brien, D. Detollenaere, R. Kaptein, B. M. Weckhuysen and W. Bras, *J. Synchrotron Radiat.*, 2008, **15**, 632–640.

37 M. Sadeqzadeh, H. Karaca, O. V. Safonova, P. Fongarland, S. Chambrey, P. Roussel, a. Griboval-Constant, M. Lacroix, D. Curulla-Ferré, F. Luck and a. Y. Khodakov, *Catal. Today*, 2011, **164**, 62–67.

38 H. Karaca, J. Hong, P. Fongarland, P. Roussel, A. Griboval-Constant, M. Lacroix, K. Hortmann, O. V Safonova and A. Y. Khodakov, *Chem. Commun. (Camb).*, 2010, **46**, 788–90.

39 N. Fischer, B. Clapham, T. Feltes, E. van Steen and M. Claeys, *Angew. Chemie Int. Ed.*, 2014, **53**, 1342–1345.

40 O. Ducreux, B. Rebours, J. Lynch, M. Roy-Auberger and D. Bazin, *Oil Gas Sci. Technol. - Rev. l'IFP*, 2008, **64**, 49–62.

41 Z.-P. Liu and P. Hu, *J. Am. Chem. Soc.*, 2003, **125**, 1958–67.

42 M. K. Gnanamani, G. Jacobs, W. D. Shafer and B. H. Davis, *Catal. Today*, 2013, **215**, 13–17.

43 V. V. Matveev, D. A. Baranov, G. Y. Yurkov, N. G. Akatiev, I. P. Dotsenko and S. P. Gubin, *Chem. Phys. Lett.*, 2006, **422**, 402–405.

44 S. Alayoglu, P. Zavalij, B. Eichhorn, Q. Wang, A. I. Frenkel and P. Chupas, *ACS Nano*, 2009, **3**, 3127–37.

45 S. J. L. Billinge, *J. Solid State Chem.*, 2008, **181**, 1695–1700.

46 C. L. Farrow, P. Juhas, J. W. Liu, D. Bryndin, E. S. Božin, J. Bloch, T. Proffen and S. J. L. Billinge, *J. Phys. Condens. Matter*, 2007, **19**, 335219.

47 H. E. du Plessis, R. P. Forbes, W. Barnard, W. J. Erasmus and A. Steuwer, *Phys. Chem. Chem. Phys.*, 2013, **15**, 11640–5.

48 A. M. Beale and G. Sankar, *Chem. Mater.*, 2006, **18**, 263–272.

49 J. M. Thomas, G. N. Greaves, G. Sankar, P. A. Wright, J. Chen, A. J. Dent and L. Marchese, *Angew. Chemie Int. Ed. English*, 1994, **33**, 1871–1873.

50 K. Høydalsvik, J. B. Fløystad, A. Voronov, G. J. B. Voss, M. Esmaeili, J. Kehres, H. Granlund, U. Vainio, J. W. Andreasen, M. Rønning and D. W. Breiby, *J. Phys. Chem. C*, 2014, **118**, 2399–2407.

51 G. Bergeret and P. Gallezot, in *Handbook of Heterogeneous Catalysis*, Wiley-VCH Verlag GmbH & Co. KGaA, 2008.

52 Z. Sun, B. Sun, M. Qiao, J. Wei, Q. Yue, C. Wang, Y. Deng, S. Kaliaguine and D. Zhao, *J. Am. Chem. Soc.*, 2012, **134**, 17653–60.

53 H. Borchert, E. V. Shevchenko, A. Robert, I. Mekis, A. Kornowski, G. Grübel and H. Weller, *Langmuir*, 2005, **21**, 1931–6.

54 W. Bras, I. P. Dolbnya, D. Detollenaere, R. van Tol, M. Malfois, G. N. Greaves, A. J. Ryan and E. Heeley, *J. Appl. Crystallogr.*, 2003, **36**, 791–794.

55 H. Guan, X. Wang, H. Li, C. Zhi, T. Zhai, Y. Bando and D. Golberg, *Chem. Commun.*, 2012, **48**, 4878.

56 P. H. T. Ngamou and N. Bahlawane, *Chem. Mater.*, 2010, **22**, 4158–4165.

57 L. E. Iton, I. Choi, J. A. Desjardins and V. A. Maroni, 1989, **9**, 535–538.

58 A. Singh and L. Spiccia, *Coord. Chem. Rev.*, 2013, **257**, 2607–2622.

59 G. L. Ott, T. Fleisch and W. N. Delgass, *J. Catal.*, 1979, **60**, 394–403.

60 G. Brodén, G. Gafner and H. P. Bonzel, *Surf. Sci.*, 1979, **84**, 295–314.

61 H. P. Bonzel and H. J. Krebs, *Surf. Sci.*, 1981, **109**, L527–L531.

62 G. F. Meyers and M. B. Hall, *Inorg. Chem.*, 1984, **23**, 124–131.

63 A. A. Verberckmoes, B. M. Weckhuysen and R. A. Schoonheydt, *Microporous Mesoporous Mater.*, 1998, **22**, 165–178.

64 A. Y. Khodakov, A. Griboval-Constant, R. Bechara and V. L. Zholobenko, *J. Catal.*, 2002, **206**, 230–241.

65 F. P. J. M. Kerkhof and J. A. Moulijn, *J. Phys. Chem.*, 1979, **83**, 1612–1619.

66 M. P. Seah and W. A. Dench, *Surf. Interface Anal.*, 1979, **1**, 2–11.

67 J. H. Scofield, *J. Electron Spectros. Relat. Phenomena*, 1976, **8**, 129–137.

68 D. G. Castner, P. R. Watson and I. Y. Chan, *J. Phys. Chem.*, 1989, **93**, 3188–3194.

69 D. F. Ogletree, H. Bluhm, G. Lebedev, C. S. Fadley, Z. Hussain and M. Salmeron, *Rev. Sci. Instrum.*, 2002, **73**, 3872.

70 S. K. Beaumont, S. Alayoglu, V. V. Pushkarev, Z. Liu, N. Kruse and G. A. Somorjai, *Faraday Discuss.*, 2013, **162**, 31.

71 V. Papaefthimiou, T. Dintzer, V. Dupuis, A. Tamion, F. Tournus, A. Hillion, D. Teschner, M. Hävecker, A. Knop-Gericke, R. Schlögl and S. Zafeiratos, *ACS Nano*, 2011, **5**, 2182–90.

72 S. Alayoglu, S. K. Beaumont, F. Zheng, V. V. Pushkarev, H. Zheng, V. Iablokov, Z. Liu, J. Guo, N. Kruse and G. A. Somorjai, *Top. Catal.*, 2011, **54**, 778–785.

73 F. De Groot, *Chem. Rev.*, 2001, 101, 1779–1808.

74 M. Fernández-García, *Catal. Rev.*, 2002, **44**, 59–121.

75 G. Jacobs, W. Ma, P. Gao, B. Todic, T. Bhatelia, D. B. Bukur and B. H. Davis, *Catal. Today*, 2013, **214**, 100–139.

76 A. Rochet, V. Moizan, C. Pichon, F. Diehl, A. Berliet and V. Briois, *Catal. Today*, 2011, **171**, 186–191.

77 G. Jacobs, J. A. Chaney, P. M. Patterson, T. K. Das, J. C. Maillot and B. H. Davis, *J. Synchrotron Radiat.*, 2004, **11**, 414–22.

78 G. Kwak, M. H. Woo, S. C. Kang, H. G. Park, Y. J. Lee, K. W. Jun and K. S. Ha, *J.*

Catal., 2013, **307**, 27–36.

79 A. M. Beale and B. M. Weckhuysen, *Phys. Chem. Chem. Phys.*, 2010, **12**, 5562–74.

80 N. E. Tsakoumis, M. Rønning, Ø. Borg, E. Rytter and A. Holmen, *Catal. Today*, 2010, **154**, 162–182.

81 J. C. Mohandas, M. K. Gnanamani, G. Jacobs, W. Ma, Y. Ji, S. Khalid and B. H. Davis, *ACS Catal.*, 2011, **1**, 1581–1588.

82 J. van de Loosdrecht, B. Balzhinimaev, J.-A. Dalmon, J. W. Niemantsverdriet, S. V. Tsybulya, A. M. Saib, P. J. van Berge and J. L. Visagie, *Catal. Today*, 2007, **123**, 293–302.

83 D. J. Moodley, A. M. Saib, J. van de Loosdrecht, C. A. Welker-Nieuwoudt, B. H. Sigwebela and J. W. Niemantsverdriet, *Catal. Today*, 2011, **171**, 192–200.

84 G. Jacobs, P. M. Patterson, T. K. Das, M. Luo and B. H. Davis, *Appl. Catal. A Gen.*, 2004, **270**, 65–76.

85 M. Benfatto, C. R. Natoli, A. Bianconi, J. Garcia, A. Marcelli, M. Fanfoni and I. Davoli, *Phys. Rev. B*, 1986, **34**, 5774–5781.

86 D. C. Edwards and S. C. B. Myneni, *J. Phys. Chem. A*, 2005, **109**, 10249–56.

87 F. Morales, F. M. F. de Groot, P. Glatzel, E. Kleimenov, H. Bluhm, M. Hävecker, A. Knop-Gericke and B. M. Weckhuysen, *J. Phys. Chem. B*, 2004, **108**, 16201–16207.

88 S. Alayoglu, S. K. Beaumont, G. Melaet, A. E. Lindeman, N. Musselwhite, C. J. Brooks, M. A. Marcus, J. Guo, Z. Liu, N. Kruse and G. A. Somorjai, *J. Phys. Chem. C*, 2013, **117**, 21803–21809.

89 G. A. Somorjai, S. K. Beaumont and S. Alayoglu, *Angew. Chem. Int. Ed. Engl.*, 2011, **50**, 10116–29.

90 T. Herranz, X. Deng, A. Cabot, J. Guo and M. Salmeron, *J. Phys. Chem. B*, 2009, **113**, 10721–7.

91 A. Tuxen, S. Carenco, M. Chintapalli, C.-H. Chuang, C. Escudero, E. Pach, P. Jiang, F. Borondics, B. Beberwyck, A. P. Alivisatos, G. Thornton, W.-F. Pong, J. Guo, R. Perez, F. Besenbacher and M. Salmeron, *J. Am. Chem. Soc.*, 2013, **135**, 2273–8.

92 V. F. Puntes, K. M. Krishnan and A. P. Alivisatos, *Science*, 2001, **291**, 2115–7.

93 V. Iablokov, S. K. Beaumont, S. Alayoglu, V. V Pushkarev, C. Specht, J. Gao, A. P. Alivisatos, N. Kruse and G. A. Somorjai, *Nano Lett.*, 2012, **12**, 3091–6.

94 Z. Yan, Z. Wang, D. B. Bukur and D. W. Goodman, *J. Catal.*, 2009, **268**, 196–200.

95 O. R. Inderwildi, S. J. Jenkins and D. A. King, *J. Phys. Chem. C*, 2008, **112**, 1305–1307.

96 F. Zheng, S. Alayoglu, J. Guo, V. Pushkarev, Y. Li, P.-A. Glans, J. Chen and G. Somorjai, *Nano Lett.*, 2011, **11**, 847–53.

97 S. K. Beaumont, S. Alayoglu, C. Specht, W. D. Michalak, V. V Pushkarev, J. Guo, N. Kruse and G. A. Somorjai, *J. Am. Chem. Soc.*, 2014, **136**, 9898–901.

98 G. Melaet, W. T. Ralston, C.-S. Li, S. Alayoglu, K. An, N. Musselwhite, B. Kalkan and G. A. Somorjai, *J. Am. Chem. Soc.*, 2014, **136**, 2260–3.

99 K. H. Cats, I. D. Gonzalez-Jimenez, Y. Liu, J. Nelson, D. van Campen, F. Meirer, A. M. J. van der Eerden, F. M. F. de Groot, J. C. Andrews and B. M. Weckhuysen, *Chem.*

Commun. (Camb)., 2013, **49**, 4622–4.

100 B. Ernst, A. Bensaddik, L. Hilaire, P. Chaumette and A. Kiennemann, *Catal. Today*, 1998, **39**, 329–341.

101 A. Y. Khodakov, J. Lynch, D. Bazin, B. Rebours, N. Zanier, B. Moisson and P. Chaumette, *J. Catal.*, 1997, **168**, 16–25.

102 D. G. Castner, P. R. Watson and I. Y. Chan, *J. Phys. Chem.*, 1990, **94**, 819–828.

103 R. Bechara, D. Balloy, J.-Y. Dauphin and J. Grimblot, *Chem. Mater.*, 1999, **11**, 1703–1711.

104 K. H. Cats, J. C. Andrews, O. Stéphan, K. March, C. Karunakaran, F. Meirer, F. M. F. de Groot and B. M. Weckhuysen, *Catal. Sci. Technol.*, 2016.

105 V. A. de la P. O'Shea, M. C. Á. Galván, A. E. P. Prats, J. M. Campos-Martin and J. L. G. Fierro, *Chem. Commun. (Camb).*, 2011, **47**, 7131–3.

106 R. P. Galhenage, H. Yan, S. A. Tenney, N. Park, G. Henkelman, P. Albrecht, D. R. Mullins and D. A. Chen, *J. Phys. Chem. C*, 2013, **117**, 7191–7201.

107 R. Reuel, *J. Catal.*, 1984, **85**, 78–88.

108 G. Jacobs, T. K. Das, Y. Zhang, J. Li, G. Racoillet and B. H. Davis, *Appl. Catal. A Gen.*, 2002, **233**, 263–281.

109 A. Vamvakeros, S. D. M. Jacques, V. Middelkoop, M. Di Michiel, C. K. Egan, I. Z. Ismagilov, G. B. M. Vaughan, F. Gallucci, M. van Sint Annaland, P. R. Shearing, R. J. Cernik and A. M. Beale, *Chem. Commun.*, 2015.

110 S. D. M. Jacques, M. Di Michiel, S. A. J. Kimber, X. Yang, R. J. Cernik, A. M. Beale and S. J. L. Billinge, *Nat. Commun.*, 2013, **4**, 2536.